ABSTRACT

COMBUSTION DYNAMICS OF METAL POWDERS IN MIXED GAS FLOWS

by
Amy Lee Corcoran

Predictive mechanisms for particle ignition and combustion rates are required in order to develop optimized propellant and energetic formulations using micron-sized metal powders, such as aluminum and magnesium. Most current descriptions are based on laboratory experiments performed in stationary or laminar combustion configurations using pure metals burned in single oxidizers. However, practical configurations take into account different metals, including alloys, that burn in various oxidizing environments and various flow conditions. Validity of the present descriptions for such environments has not been established. This experimental study is aimed to measure burn times for aluminum, magnesium, and mechanically alloyed Al·Mg particles burning in different oxidizing environments; for aluminum and the mechanically alloyed Al·Mg alloys, turbulence is varied. The first environment consists of a laminar air-acetylene flame; auxiliary tangential jets of air with adjustable flow rates are used to achieve different controlled levels of turbulence. The second environment consists of a hydrogen/oxygen diffusion flame. In both cases, metal powder is injected in the flame axially using a flow of nitrogen. Aluminum powder is studied in both environments while magnesium is purely studied in the hydrogen/oxygen diffusion flame and the mechanically alloyed powders are studied in the combustion products of an air/acetylene flame. For the initial experimental data collection, aluminum streaks of burning particles are photographed using a camera placed behind a mechanical chopper interrupting the photo-exposure with

a pre-set frequency. The obtained dashed streaks are used to measure the particle burn times for different flow conditions. The second experimental data collection includes filtered photomultiplier tubes which capture particle emission durations that represent the particle burn times. The particle burn times are correlated with the particle size distribution to obtain the burn time as a function of the particle size assuming larger particles burn longer. It is expected that these results will serve to develop a mechanistic model for burn rates of Al, Mg, and Al·Mg alloys in various gas environments.

COMBUSTION DYNAMICS OF METAL POWDERS IN MIXED GAS FLOWS

by
Amy Lee Corcoran

A Thesis
Submitted to the Faculty of
New Jersey Institute of Technology
in Partial Fulfillment of the Requirements for the Degree of
Master of Science in Chemical Engineering

Otto H. York Center Department of
Chemical, Biological and Pharmaceutical Engineering

January 2015

APPROVAL PAGE

COMBUSTION DYNAMICS OF METAL POWDERS IN MIXED GAS FLOWS

Amy Lee Corcoran

Dr. Edward L. Dreizin, Dissertation Advisor — Date
Professor of Chemical Engineering, NJIT

Dr. Robert B. Barat, Committee Member — Date
Professor of Chemical Engineering, NJIT

Dr. Mirko Schoenitz, Committee Member — Date
Associate Research Professor of Chemical Engineering, NJIT

BIOGRAPHICAL SKETCH

Author: Amy Lee Corcoran

Degree: Master of Science

Date: January 2015

Undergraduate and Graduate Education:

- Master of Science in Chemical Engineering,
  New Jersey Institute of Technology, Newark, N.J., 2015

- Bachelor of Science in Chemical Engineering,
  New Jersey Institute of Technology, Newark, N.J., 2015

Major: Chemical Engineering

Publications:

Corcoran, A.L., Wang, S., Aly, Y., Dreizin, E.L. "Combustion of mechanically alloyed Al·Mg powders in products of a hydrocarbon flame". *Combustion Science and Technology* (In Press)

Wang, S., Corcoran, A.L., Dreizin, E.L. "Combustion of magnesium powders in products of an air/acetylene flame". *Combustion and Flame* (In Press)

Corcoran, A.L., Mercati, S., Nie, H., Milani, M., Montorsi, L., Dreizin, E.L. "Combustion of fine aluminum and magnesium powders in water". *Combustion and Flame* 160(10) pp. 2242-2250 (2013)

Corcoran, A.L., Hoffman, V.K., Dreizin, E.L. "Aluminum particle combustion in turbulent flames". *Combustion and Flame* 160(3) pp. 718-724 (2013)

Presentations:

"Combustion Dynamics of Metal Powders in Various Flame Environments", Women in Engineering Event at Westwood Regional Jr./Sr. High School, April 2014

"Combustion of Metal Powders in Mixed Gas Flows", DTRA Annual Meeting, July 2014

"Combustion Dynamics of Mechanically Alloyed Al·Mg Powders in Turbulent Flames", SWE First Annual Female Research Showcase, February 2014

"Combustion Dynamics of Mechanically Alloyed Al·Mg Powders in Turbulent Flames", AIChE Annual Meeting, November 2013

"Combustion of Metal Powders in Mixed Gas Flows", DTRA Annual Meeting, July 2013

"Aluminum Particle Combustion in Turbulent Flames", Undergraduate Research Symposium: NJIT, February 2013

"Combustion Dynamics of Aluminum in Turbulent Flows", AIChE Annual Meeting, November 2012

"Aluminum Particle Combustion in Turbulent Flames", DTRA Annual Meeting, July 2012

"Aluminum Combustion in Turbulent Flames", AIAA Regional Conference: SUNY, April 2012

This thesis is dedicated to my wonderful husband, Timothy McSparron
and my lovely sister, Erin Corcoran.
Thank you for your unconditional love and support.

ACKNOWLEDGMENT

It is with great respect and admiration that I acknowledge the support of Dr. Edward L. Dreizin for his continuous support throughout my undergraduate and graduate career. His patience and guidance helped me achieve my research goals. Dr. Dreizin's kindness and thirst for knowledge is unsurmountable. Without his excellent teaching and leadership qualities along with his extensive intelligence, this thesis would not have been possible.

I would also like to acknowledge my committee members, Dr. Robert Barat and Dr. Mirko Shoenitz. Dr. Barat's kindness and constant positive attitude let me know that I can achieve greatness. Dr. Shoenitz reminded me that I can always have fun in the laboratory and that no question is ever too stupid to ask. He also taught me that with scraps, a little elbow grease, and a creative mind that anything can be built.

The Defense Threat reduction Agency deserves a thank you for their support to which this research would not have started. Their annual meetings gave me a glimpse of what future researchers are capable of doing in the field of energetics.

I would like to thank my fellow lab mates for their help especially when equipment seemed to just fall apart. Their friendships made work enjoyable and just that much more exciting. My next work team has some pretty big shoes to fill.

Last, but not least, I'd like to thank my family. Without my parents, Carol and James Corcoran, pushing me to go to college this train would've never started. Your support and understanding made me who I am. My sister deserves a "thank you" for listening when I needed someone to talk to about those challenging days. Also, my husband Tim and our dog Tony deserve a huge thank you for the warm greetings on difficult days.

TABLE OF CONTENTS

TABLE OF CONTENTS
(Continued)

Chapter **Page**

LIST OF TABLES

LIST OF FIGURES

LIST OF FIGURES
(Continued)

LIST OF FIGURES
(Continued)

Figure **Page**

LIST OF FIGURES
(Continued)

Figure **Page**

CHAPTER 1

ALUMINUM PARTICLE COMBUSTION IN TURBULENT FLAMES

1.1 Introduction

Metal powders are used as fuel additives in many energetic formulations including propellants [1-3], explosives [4-9], and pyrotechnics [10-13]. In most practical configuration, combustion of metal particles occurs in turbulent flows [14-18], commonly involving hydrocarbon combustion products mixed with surrounding atmosphere. Performance of such energetic systems is described using advanced hydrodynamic codes [19-22] which evaluate contribution of metal particle combustion using simplified submodels. The most commonly used metal additive for energetic formulations is aluminum, and many current submodels for aluminum combustion are based on experiments reviewed in Ref. [23], using primarily coarse, 50 – 250 μm particles burning under well-characterized, laminar laboratory conditions. Thus, despite the advanced capabilities of contemporary hydrocodes in describing the flow and mixing patterns containing burning aluminum particles, the effect of these conditions on the burn rate remains unaccounted for. Experimental studies of the effect of turbulence on metal combustion are relatively scarce and all involve dust explosions [24-27], yielding correlations between turbulence and observed pressures and rates of pressure rise, which are difficult to interpret in terms of individual particle burn rates. On the other hand, useful correlations for the effect of turbulence on evaporation rate of liquid fuel droplet have been developed and reviewed in Ref. [28]. A simple correction for the droplet vaporization rate under turbulent convective flow, K_t, is proposed as:

$$\frac{K_t}{K_l} = 1 + CI + C_{Frö}\,\mathrm{Re}_d^{1/2}\,Sc^{1/3} \tag{1.1}$$

where K_l is the average vaporization rate under laminar flow conditions, C is a constant, I is turbulence intensity, and the last term on the right hand side gives Frössling's correlation for the vaporization rate in laminar flow conditions estimated based on the vaporization rate in stationary environment. It includes Frössling's coefficient $C_{Frö} \approx 0.18$ multiplied by Re_d, the Reynolds number based on the particle diameter, and by Sc, the Schmidt number. The value of turbulence intensity, I, is defined as:

$$I = \frac{u'}{U} \tag{1.2}$$

where U is the longitudinal mean velocity component and u' is root mean square of the fluctuating velocity component along the transversal flow direction. An expression similar to Equation (1.1) which corrects the metal particle burn rate as a function of the turbulence intensity would substantially improve the predictive accuracy of hydrocodes dealing with metal combustion. However, no data necessary to obtain such an expression could be found in the literature. This paper is aimed to begin generating such experimental data and thus to begin quantifying the effect of turbulent flow conditions on the metal particle combustion.

1.2 Experimental

1.2.1 General Approach

The experimental setup is schematically shown in Figure 1.1 Aluminum powder is fed through an air-acetylene flame. The particles ignite and burn in the combustion products of the hydrocarbon flame, while surrounding air is mixed in the combustion environment,

providing additional oxidizer. Initial flame and particle flow are directed vertically. The turbulence is introduced by three auxiliary nozzles placed horizontally around the flame and directed tangentially within a short cylindrical enclosure. Air is fed through auxiliary nozzles at a controlled rate, enabling one to adjust the level of the achieved turbulence. This method of producing turbulence is similar to the method used in Refs. [29, 30], where tangentially directed fans were installed inside an explosion vessel. In addition to the new flow pattern, this approach enhances mixing of the flame and burning particles with the surrounding air. These two effects cannot be separated from each other in the present experiment. Note, however, that the situation is analogous for a fireball produced by a metallized explosive and expanding in air: turbulent mixing of the fireball with its surroundings affects both flow pattern and gas composition to which the metal particles within the expanding fireball are subjected. The gross effect of this turbulent mixing on the particle combustion rate is of substantial interest, and this effect is explored here.

The particle burn times are measured as a function of the produced turbulence level. The burn times are obtained from the streaks produced by incandescent particles. The streaks are photographed through a rapidly spinning disk with multiple holes made along its circumference (chopper) so that the streak images appear dashed, and the number of dashes per streak can be used to determine the burn time. A statistical distribution of the burn times is correlated with the measured particle size distribution to obtain the particle burn times as a function of their diameters. Note that most particles ignite while being introduced into the laminar flame zone and continue burning passing through the turbulent regions. The measured burn times do not discriminate between these, possibly different combustion regimes. Different particles arrive into the flow

regions affected by turbulent mixing at different stages of their combustion. The precise instant when each particle becomes affected by turbulent mixing depends on at least two parameters: particle size and its axial coordinate. Larger particles tend to have longer pre-heating times; particles located further away from the jet's center tend to ignite sooner because of greater oxidizer availability. Neither particle size nor its exact axial location could be measured directly, thus meaningful analysis of the respective data where the "laminar" and "turbulent" burn times are separated would be impossible. Once again, of interest is the gross effect of turbulence on the burn times of metal particles, and it is addressed in the present experiments.

Photographed particle streaks are also used to quantify the turbulence intensity. When a vertically rising particle reaches the turbulent region, its trajectory is observed to curve. From the observed trajectory curvature, acceleration is estimated. The particle mass is evaluated based on its measured burn time and the above mentioned correlation between the burn time and particle size. Finally, the drag force is estimated using the particle mass and acceleration; the force is assumed to be directly proportional to the transversal flow velocity based on the Stokes equation. Thus, the value of the transversal component of the gas velocity curving a particle's vertical trajectory is obtained. The longitudinal component of the gas velocity is also obtained from the photographed particle streaks assuming that the particles follow the gas flow prior to entering the turbulent region.

Further details of the experimental apparatus and procedure are described below.

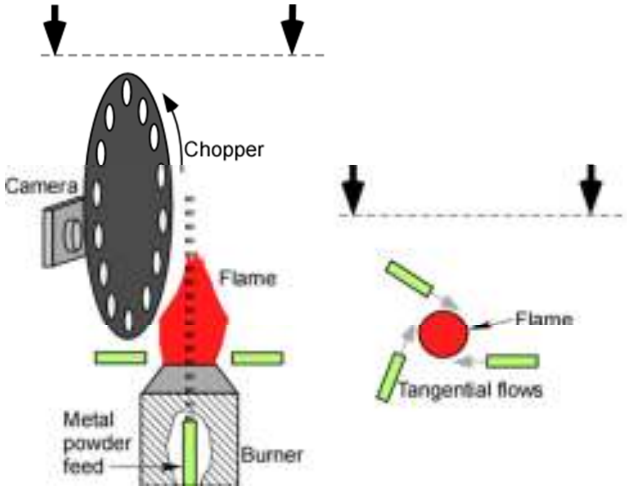

Figure 1.1 Schematic diagram of the experimental setup.

1.2.2 Powder Feeder

The powder feeder was designed around the concept of creating an aerosol from directing a high velocity gas jet on a powder loaded into the threads of a screw (Figure 1.2). In this design, the aerosol jet velocity is controlled by the flow rate of the carrier gas. The mass feed rate of the powder is adjusted separately, by changing the thickness of the coating and rate of the screw rotation.

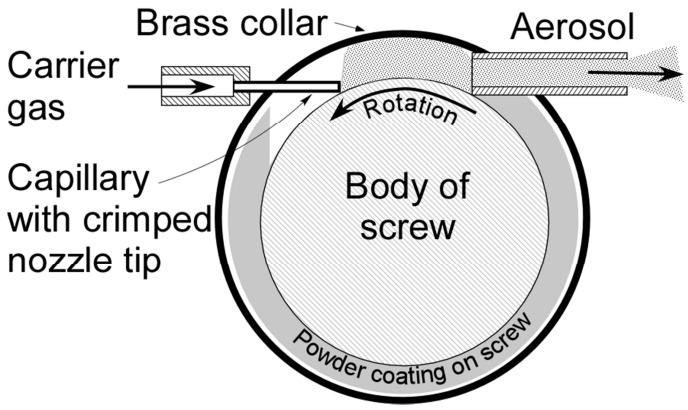

Figure 1.2 Schematic diagram of powder feeder.

A stainless steel screw, ¾" (19.05 mm) diameter with 16 threads per inch was used. To coat the screw with powder, the dry powder was placed in a plastic dish. The mass of the powder was measured and recorded. Using a short bristle brush, the powder was deposited into the threads of the screw. After the powder had been applied, the remaining weight was recorded so that the total mass of the sample to be used in experiments was determined. The screw loaded with powder was then placed into the feeder assembly, including a cylindrical brass collar (see Figure 1.2) and a coupling connecting it with the motor.

The brass collar has feedthroughs for the carrier gas inlet and aerosol outlet. A brass capillary tube (1/16" or 1.59 mm OD) inserted through the carrier gas inlet, was crimped to make a triangular nozzle tip (~0.62 mm on each side) that conforms to the "V" channel of the screw threads. Nitrogen was used as carrier gas. The nozzle tip directs a high velocity nitrogen jet into the thread to efficiently remove and aerosolize the powder. The aerosol exits through an opposing small diameter brass tube on the feed screw collar (inserted into the aerosol outlet feedthrough). The brass collar together with the aerosol outlet move along the screw during the operation. The aerosol outlet is connected to the burner using flexible plastic tubing. The nitrogen feed rate is measured using a rotameter.

The rotational speed of the screw controls the amount of powder that is aerosolized and fed into the burner. The feed screw is coupled with a knuckle joint to a speed reduction gear train driven by a DC motor. Through these gears, the motor provides a nominal operating range of 0-1.9 RPM. The motor speed is controlled by a voltage regulated, 0-30 VDC power supply.

A typical powder load was 2.6 g, which was placed over about 10-cm length of the screw. In preliminary tests, various voltages and respective powder feed rates were tested. The voltage selected, 4 V, fed enough of the powder into the burner to obtain multiple particle streaks in each flame image. A higher voltage fed too many particles, so that the images became saturated. A lower voltage fed too few particles and it was difficult to identify their streaks in most flame images.

1.2.3 Burner

A schematic diagram of the steel burner and enclosure used to generate turbulent flow patterns is shown in Figure 1.3. Acetylene and air are fed through a tube with narrowed internal diameter. Fine brass screens were installed to enhance mixing. A thin stainless steel tube placed at the axis of the burner was used to inject the particles carried by nitrogen. The flame shape is sensitive to the position of the central tube, which must be carefully centered to achieve the desired symmetric flame configuration. The produced flame is laminar. To generate turbulence, the flame needs to be disturbed or agitated. This is achieved by directing three tangential air jets around the flame. The burner is equipped with an attachment including three nozzles directed tangentially inside a hollow cylinder. The burner is placed inside the cylinder, and the air flow is adjusted to create the desired level of turbulence. Individual rotameters are used to monitor air, acetylene, and air flow rates.

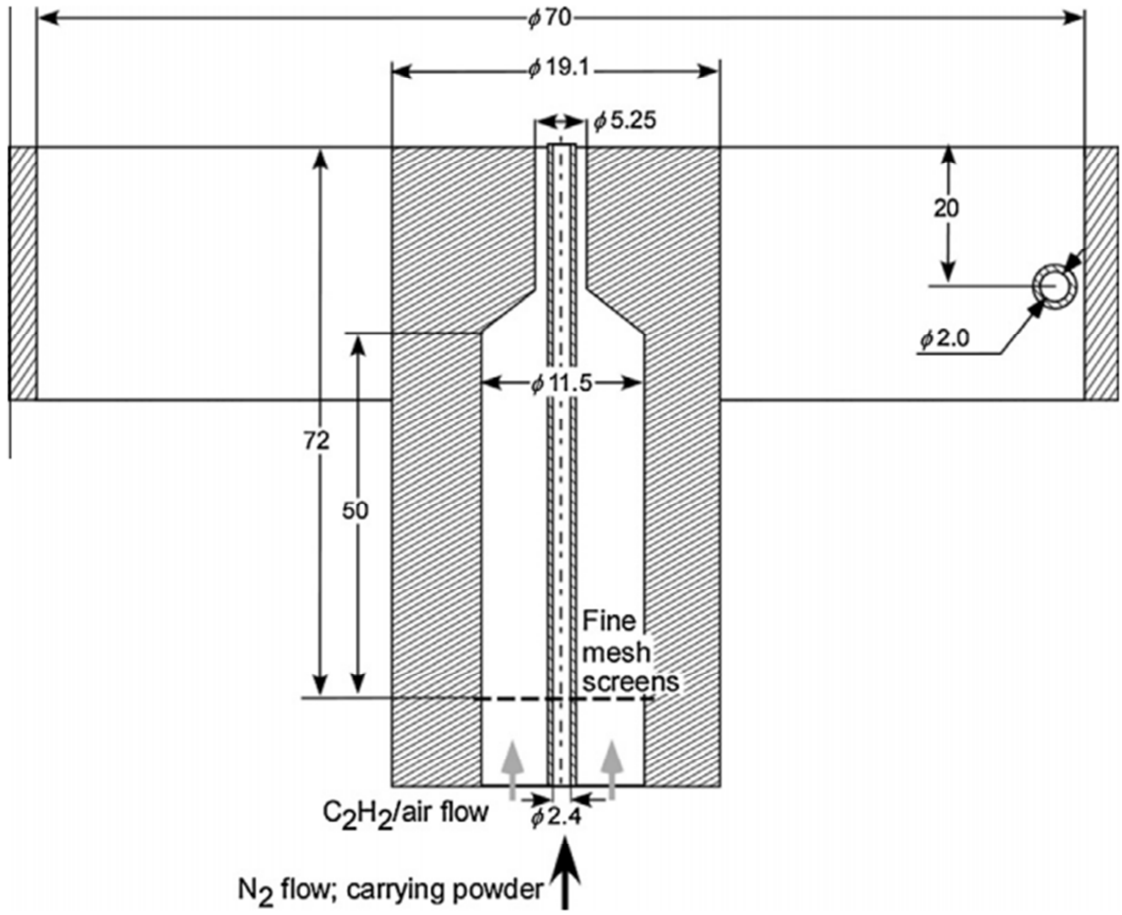

Figure 1.3 Schematic diagram of the burner together with enclosure and one of the turbulent-generating nozzles. All dimensions are in mm.

1.2.4 Material

A spherical aluminum powder designated as X-65 by the manufacturer, Alcan-Toyo America Inc., was used. The particle size distribution for this powder was measured using a Beckman-Coulter LS230 Enhanced Particle Analyzer and is shown in Figure 1.4. This size distribution was used to process experimental data, as described below.

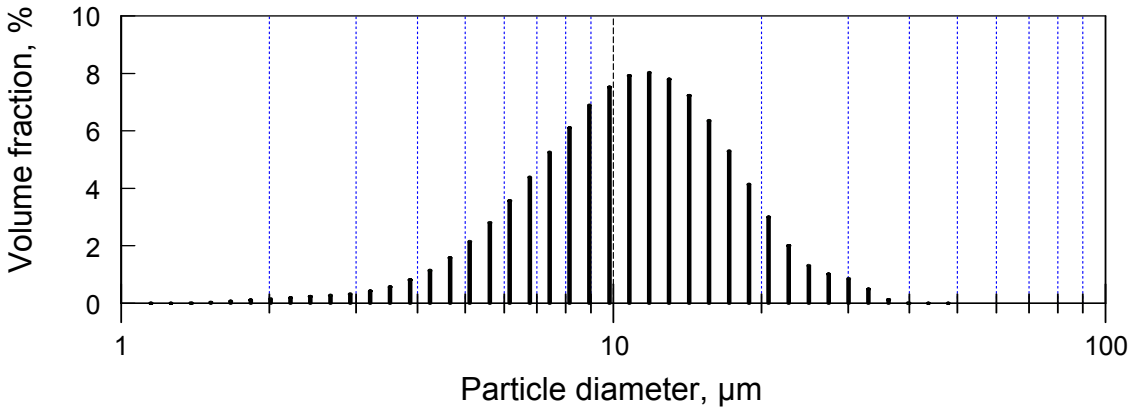

Figure 1.4 Particle size distribution for X-65 aluminum powder used in experiments.

1.2.5 Images and Image Processing

The images were taken using a DSC-H50 camera set at a shutter speed of 1/60 s and an aperture of f/8.0. A chopper disk attached to a motor was installed in front of the camera. The chopper was a 12 cm diameter disk with 36 holes of equal diameter made along its circumference. In preliminary tests, a light source was placed in front of the chopper and a photodiode was placed behind it to calibrate the chopping time interval adjusted by the motor speed. The chopping period, τ = 0.21 ms was used in experiments (corresponding to the motor speed of about 8000 rpm). Thus, each image taken during 1/60 s included 79 exposures.

A characteristic flame image with particle streaks is shown in Figure 1.5. The particle streaks appear above the premixed (bright) portion of the air-acetylene flame. Initially, the particles move nearly vertically, but when they reach a turbulent zone, their trajectories curve. Several images with top views of the flame and burning particle streaks are shown in Figure 1.6. The latter images were taken without the chopper disk. At different instants when different images in Figure 1.6 were taken, particles move away from the flame in different directions. We observed no selected direction in which the particles would be preferentially deflected; there was also no detectable swirling pattern

formed by particle streaks. Side view images of the flame, as in Figure 1.5 were processed further. For each image, all clearly discernible streaks were identified, and the number of dashes per streak was calculated. The overlapping or partially visible streaks were discarded. For each flow condition, at least 200 images were taken for processing.

In order to determine the transversal flow velocity, necessary for assessing the turbulence level, a location where particle trajectories were curved was visually identified. For that location, particle coordinates for three sequential exposures (defined by the chopper positions) were measured, as illustrated in Figure 1.7. Note that only particles remaining in focus during their entire observed trajectories were considered, so that the changes in their velocity component directed towards or away from the camera were negligible. The camera was focused at the center axis of the burner and the depth of the focal field was about 10 mm. The camera was about 200 mm away from the flame. A large inset in Figure 1.7 shows a portion of the flame image with several streaks. A small inset shows the portion of the image where the curving of the particle trajectory began so that three sequential locations for a selected particle were identified and characterized. Both longitudinal, U, and transversal, u, particle velocities were determined before and after the trajectory started to curve (subscripts 1 and 2, respectively) as:

$$U_1 = \frac{\Delta y_1}{\tau}; \quad U_2 = \frac{\Delta y_2}{\tau};$$
$$u_1 = \frac{\Delta x_1}{\tau}; \quad u_2 = \frac{\Delta x_2}{\tau} \tag{1.3}$$

The average value between U_1 and U_2 was used as U. Note that the values of U_1 and U_2 were typically close to each other (and much greater than the slip velocity, estimated to be less than 1mm/s for 10 μm particles). The transversal acceleration was then obtained as

$$a = \frac{u_2 - u_1}{\tau} \tag{1.4}$$

Finally, the transversal gas velocity *u'* was determined assuming that this acceleration is produced by Stokes force, so that

$$ma = 6\pi\eta r u' \tag{1.5}$$

where m is the particle mass and η is the gas viscosity estimated at the gas surrounding temperature (assumed to be close to 1160 K). The obtained value of u' characterizes only one of two components of the transversal gas velocity. However, it was assumed to represent the value of u' adequately because of the cylindrical symmetry of the turbulence-generating flow. This assumption is further supported by radially expanding particle trajectories shown in Figure 1.6. Note that the longitudinal particle velocities (varied around 4 m/s for individual particles) were, as expected, very close to the gas velocity estimated based on the measured gas flow rates. The ratio of u'/U_1 was taken as the turbulence intensity, I, in this work.

Figure 1.5. A characteristic side view image of a flame with burning Al particle streaks. The flow rates are: acetylene: 0.9 SCFH (standard cubic feet per hour), air: 10 SCFH, nitrogen: 2 SCFH. Turbulizing air flow is set at 100 SCFH.

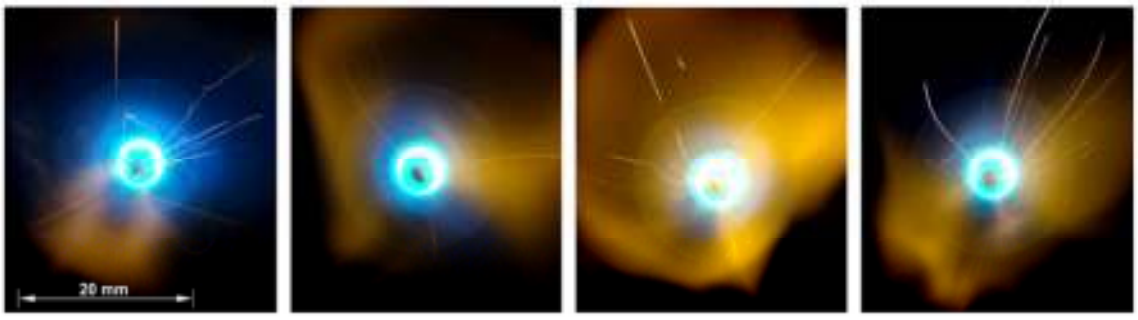

Figure 1.6. Characteristic top view images of a flame with burning Al partcle streaks. The flow rates are: acetylene: 0.9 SCFH (standard cubic feet per hour), air: 10 SCFH, nitrogen: 0.2 SCFH. Turbulizing air flow is set at 100 SCFH.

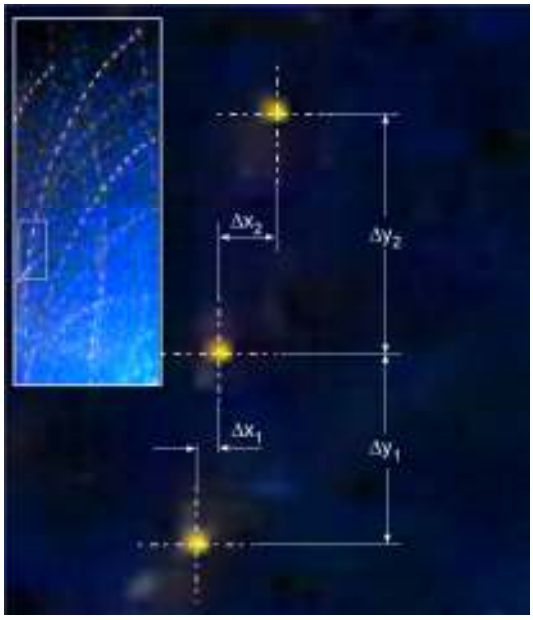

Figure 1.7. A fraction of the image used to determine particle longitudinal velocity and transversal acceleration used to quantify the turbulence level. A large inset shows a fragment of the flame image and the small inset shows the subregion selected to determine the particle velocities.

1.3 Results

The turbulence intensities for the turbulizing flows at 50 and 100 SCFH were respectively 0.031 and 0.080. These are values averaged over 12 particle streaks analyzed for each flow condition.

The burn time measurements are presented as histograms showing the number of particles versus their burn times broken into 18 bins. The bin times were selected in the logarithmic scale. The histograms are shown in Figure 1.8 for the experiments performed at different turbulence levels. It is clear that the higher level of turbulence results in a shorter burn times.

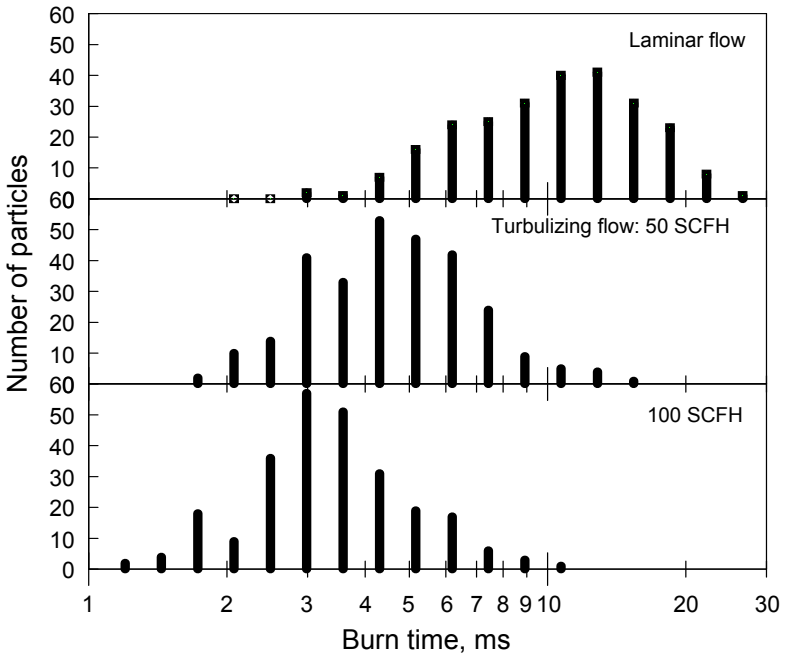

Figure 1.8 Histogram summarizing burn time measurements for experiments at different turbulence levels.

Using the data from Figure 1.4 and 1.8, burn times could be directly correlated with the particle sizes. First, the volume-based particle size distributions shown in Figure 1.4 were transferred into number-based distributions to be directly comparable to the data shown in Figure 1.8. A plot for cumulative particle number density was obtained as shown by circles in Figure 1.9. For convenience, the trend shown in Figure 1.9 was fitted using a lognormal function, describing the particle diameter as a function of the cumulative particle number density, N_d:

$$N_d = \frac{1}{2} + \frac{1}{2} erf\left[\frac{\ln(d) - \ln(\tilde{d})}{\sigma\sqrt{2}}\right] \tag{1.6}$$

where parameters σ and $\tilde{d}$ were found to be respectively, 0.66 and 3.75 μm. The fitting used the Levenberg-Marquardt algorithm in PSIplot software. The fitting function is also shown in Figure 1.9. The identified fitting function was used to recalculate the values of

particle diameters corresponding to the measured number (or number densities) of particles in each of the bins shown in Figure 1.8. In other words, for each burn time bin shown in Figure 1.8, corresponding cumulative particle number density was obtained. Using Figure 1.8, for each such value of the cumulative particle number density, respective particle diameter was found.

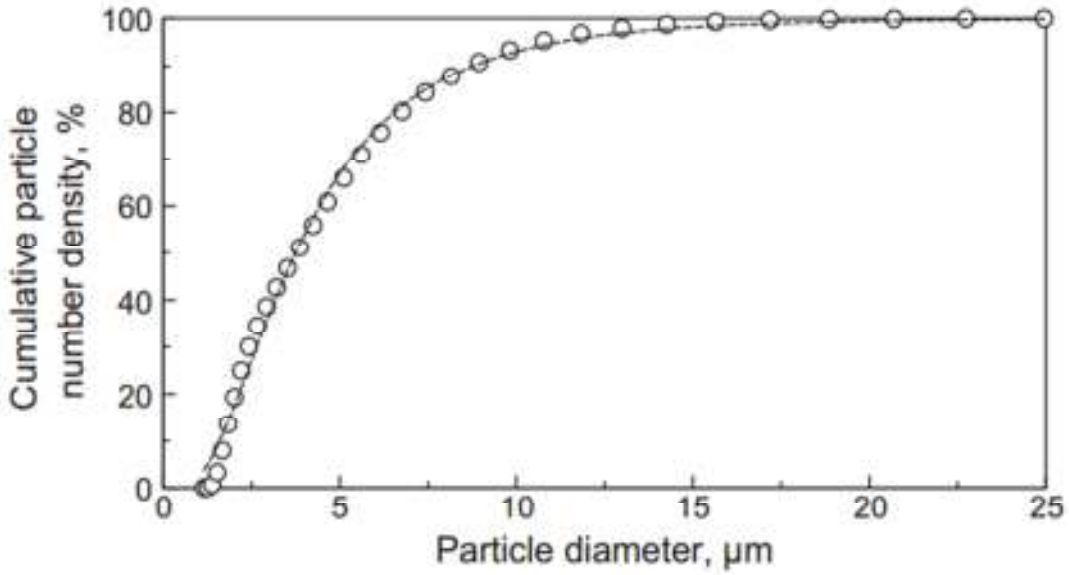

Figure 1.9 Cumulative percentage of particle number versus particle diameter obtained from data in Figure 1.4. Dashed line shows a fitting function.

The resulting plot is shown in Figure 1.10. For comparison, the burn times from Ref. [23] are also shown where an equation for particle burn time (in ms) is proposed:

$$t_b = \frac{ad^n}{X_{eff} p^{0.1} T_0^{0.2}} \tag{1.7}$$

where X_{eff} is effective oxidizer concentration, p=1 atm, is pressure, T_0 =298 K is the ambient temperature, n = 1.8 is exponent, and a = 0.00735, is a constant. The diameter, d,

is entered in μm. The effective oxidizer concentration is calculated following Ref. [23] as:

$$X_{eff} = C_{O_2} + 0.533 C_{H_2O} + 0.135 C_{CO_2} \tag{1.8}$$

where C_{O_2}, C_{H_2O}, and C_{CO_2} stand for concentrations of the respective oxidizers. Two calculations were performed using Equations (1.7) and (1.8) assuming that oxidizer is oxygen in air (X_{eff}= 0.2) or assuming that the particles burn in the combustion products of the fully reacted oxygen and acetylene:

$$C_2H_2 + 2.5O_2 \rightarrow H_2O + 2CO_2 \tag{1.9}$$

In the latter case, the combined concentrations of H_2O and CO_2 were assumed to be equal to that of the oxygen initially contained in air and consumed by acetylene, respectively:

$$X_{eff} = 0.2\left(0.533 \cdot \frac{1}{3} + 0.135 \cdot \frac{2}{3}\right) = 0.0535 \tag{1.10}$$

As shown in Figure 1.10, the correlation presented in Ref. [23] substantially underestimates the particle burn times compared to the experimental data. This result is consistent with recent measurements using a shock tube experimental apparatus [31] and experiments dealing with laser-ignited individual aluminum particles [32-34]. Fitting lines for the experimental points were obtained using d^n rate law, in which the particle burn time is proportional to their diameters in power n. All sets of experimental points were described with the d^n rate law with $n \approx 0.3 \pm 0.1$.

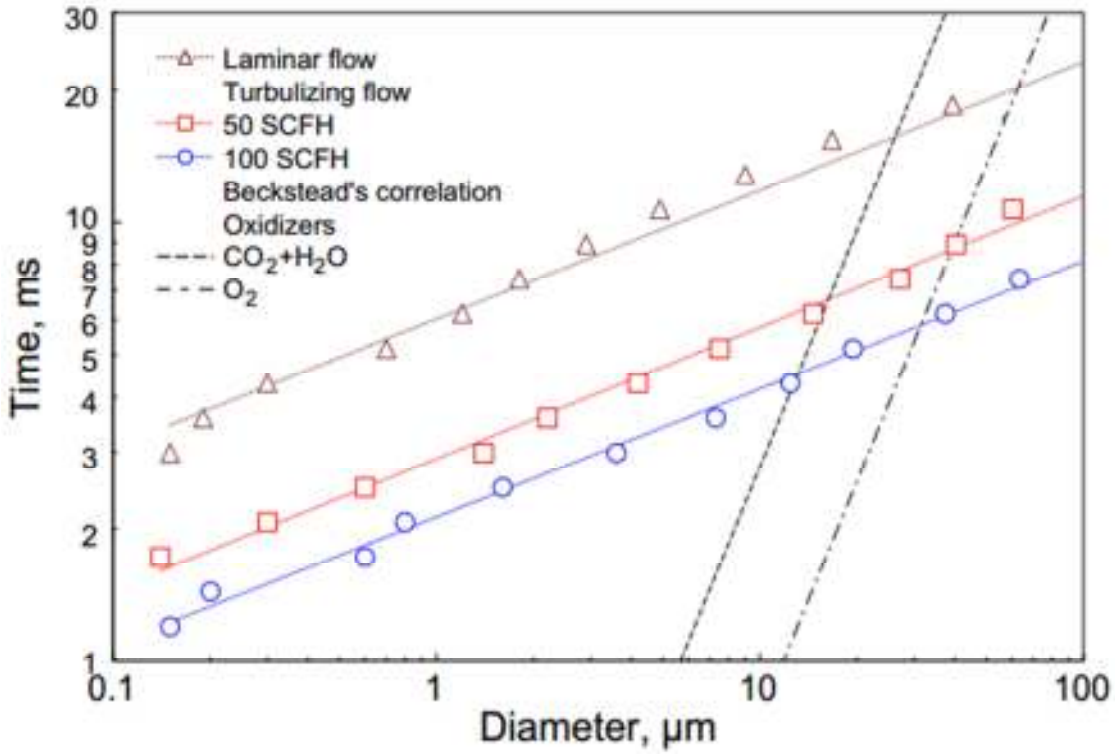

Figure 1.10. Particle burn times versus their size [23].

1.3.1 Correlation for the Burn Rate

The burn rate, $\dot{m}$, in g/s was roughly estimated as the mass of particle divided by its total burn time. For each particle size, the particle mass was obtained using aluminum density of 2.7 g/m^3. Recasting experimental data from Figure 1.10 in terms of burn rates is shown in log-log scale in Figure 1.11. The best fit for each of the experimental data point sets was found using a power function:

$$\dot{m} = K \cdot d^n \tag{1.11}$$

where K and n were adjustable parameters and particle diameter, d, was taken in μm. The best fit lines are shown in Figure 1.10. For all data sets, the value of n = 2.69 was identified. The values of the rate coefficients K are given in Table 1.1 for different turbulence intensities.

Table 1.1 Turbulence Intensities

Turbulizing flow rate, SCFH	*0*	*50*	*100*
Turbulence intensity, *I*	0	0.036	0.080
Rate coefficient, $K\times10^{-10}$[g/(s·μm$^{2.64}$)]	2.08	3.40	5.18
K_t/K_l	1	1.63	2.49

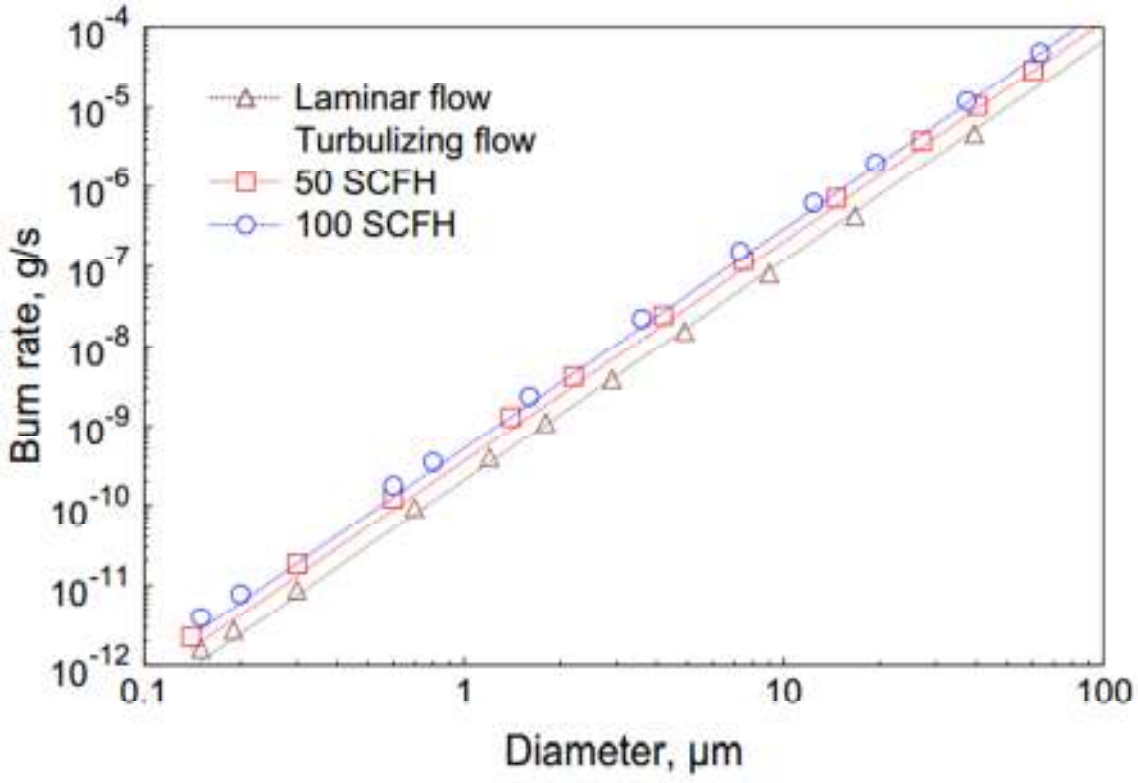

Figure 1.11 Burn rates for Al particles at different turbulence levels.

For practical situations, it is useful to obtain a correction accounting for the effect of turbulence similar to Equation (1.1). For the present experimental situation, the values

of Re_d are very small, close to 0.041 and 0.042 for turbulence intensities of 0.036 and 0.080, respectively. The value of Schmidt number is close to 1, so that the last term in Equation (1.9) becomes much smaller than 1 and can be neglected. Thus, a simplified expression for the burn rate correction is:

$$\frac{K_t}{K_l} = 1 + CI \tag{1.12}$$

Using Equation (1.12), one can find the value of coefficient C for both turbulence intensities used in the present experiments. Based on the values from Table 1.1, one finds that the for the turbulence intensities of 0.036 and 0.080, the values of C are 17.6 and 18.6, respectively. These values are quite close to each other, suggesting that using an average of C ≈ 18.2 in Equation (1.12) provides a reasonably accurate correlation for the burn rate as a function of the turbulence intensity.

CHAPTER 2

COMBUSTION OF FINE ALUMINUM AND MAGNESIUM POWDERS IN WATER

2.1 Introduction

Metal powders have high combustion enthalpies and thus are widely used as components for pyrotechnics, explosives, and solid propellants for both air and underwater propulsion systems [35-40], where they react with such oxidizers as O_2, CO_2, and H_2O. More recently, both low- and high-temperature reactions of metals with water were explored in systems aimed at producing hydrogen and electric energy, with most studies focused on Al and Mg [39-50]. Compared with the traditional hydrogen production plants based on natural gas steam reforming, producing CO_2 with rates close to 7.5 $kgCO_2/kgH_2$, the systems based on metal/water combustion are theoretically free of greenhouse gas emission [42, 44, 45].

Design of both traditional energetic systems involving combustion of Al and Mg and novel hydrogen and energy generating plants requires detailed understanding and quantitative description of dynamics of respective combustion processes. However, there are relatively few studies presenting quantitative data on burn rates of Al and Mg in water. Most of the published reports present experimental data and correlations derived for coarse metal particles, e.g., particles coarser than 20 μm were used in Refs. [23, 51], and 50-μm particles were used in Refs. [51-53]. A popular correlation proposed by M. Beckstead [23] for burn times of aluminum particles in different environments is largely based on experiments with coarse powders. The correlation might not remain useful for fine particles, although fine particles will likely be employed in practical systems, where

dimensions of the combustion chambers are limited, and thus shorter reaction times are desired. Reactions of fine aluminum particles in a heated steam were recently addressed using a shock tube [31, 54] and laser ignition experiments [33]. In the shock tube studies, aerosolized particle clouds reacted in high temperature water (2650 K) at elevated pressures (4 to 13 atm). The burn times were recovered for the entire clouds, based on their emission signatures. In laser ignition tests, individual particles burned in a gas composed of 77% of water and 23% of nitrogen and heated slightly above the water boiling point. Additional measurements focused on the effect of aluminum particle size on its burn rate are desired in environments with different concentrations of water. We were unable to find reports on combustion of fine magnesium particles in water.

The present research investigates the dynamics of combustion of aluminum and magnesium powders in high temperature water environment (around 2500 K), generated by a H_2/O_2 flame, at atmospheric pressure.

2.2 Experimental

2.2.1 Approach

Experiments were performed with fine powders of aluminum and magnesium. Particles were injected into products of a hydrogen/oxygen flame as schematically shown in Figure 2.1. Particle emission signatures were recorded using an array of four photomultiplier tubes (PMT's) equipped with interference filters [33]. Assuming that larger particles burn longer the measured distribution of particle burn times was correlated with the distribution of particle sizes. A Computational Fluid Dynamics (CFD) model was developed to describe the oxidizing environment for the present experiments.

The fiber optics bundle connected to the PMT array was placed about 50 mm away from the burner and about 30 mm above its top. This placement produced optimal results for capturing emission from entire particle streaks while minimizing the noise produced by the flame. The PMT outputs were recorded and saved at a rate of 100,000 samples per second using a 16-bit PCI-6123 data acquisition board by National Instruments and Lab-view software. The data were processed using a custom Matlab code.

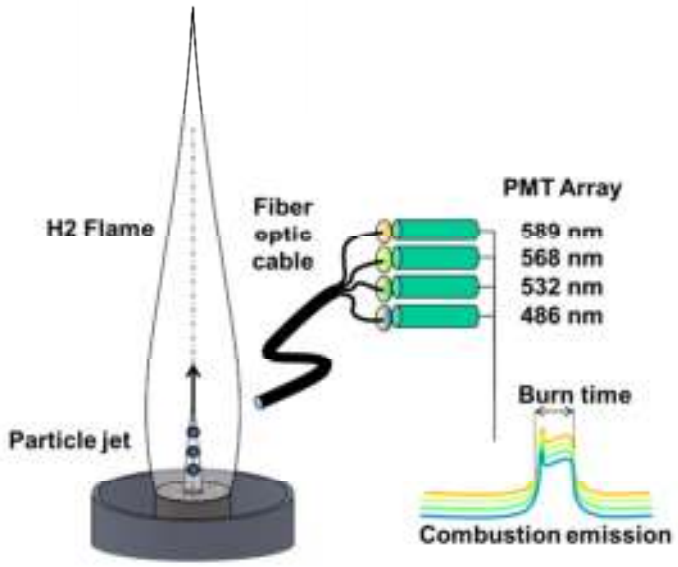

Figure 2.1 Schematic of the experimental apparatus.

2.2.2 Powder Feeder

A custom screw feeder described in more detail elsewhere [55] was used to feed the metal particles into the burner. To coat the screw with powder, the dry powder was placed in a plastic dish and weighed. Using a short bristle brush, the powder was deposited into the threads of a stainless steel, ¾" (19.05 mm) diameter screw with 16

threads per inch. A typical powder load was 0.2 g, which was placed over about 8-cm length of the screw. After the powder had been applied, the remaining weight was recorded to determine the sample mass to be used in experiments. The screw loaded with powder was then placed into a cylindrical enclosure and attached to a DC-motor. A narrow nitrogen jet blowing across a thread of a loaded screw removed powder coating and fed it into the burner. The feed rate of powder was determined by the rotational speed of the screw. It was pre-selected in preliminary experiments to ensure production of as many particle streaks as possible during the data acquisition time while minimizing overlapping peaks produced by multiple particles burning simultaneously.

2.2.3 Burner

The design and dimensions of the burner are shown in Figure 2.2. A thin stainless steel tube placed at the center of the burner is used to inject particles from the powder feeder carried by nitrogen flowing at 3.07 standard cubic feet per hour (SCFH) or 1.45 l/min. The nitrogen flow is surrounded by a flow of hydrogen fed through a tube with narrowed internal diameter at 9.04 SCFH (4.27 l/min). Oxygen flow is produced around the hydrogen flow to prevent the particles from reacting with oxygen directly. Oxygen is fed at 12.22 SCFH (5.77 l/min) through the outer cylinder of the burner. The outer cylinder contains several layers of 3-mm diameter steel balls (top layer shown at the bottom of Figure 2.2) that help in producing a laminar oxygen flow. The flame shape is sensitive to the position of the central tube carrying the nitrogen flow, which must be carefully centered to achieve the desired symmetric flame configuration. The produced flame is laminar. Individual rotameters are used to monitor hydrogen, nitrogen, and oxygen flow rates.

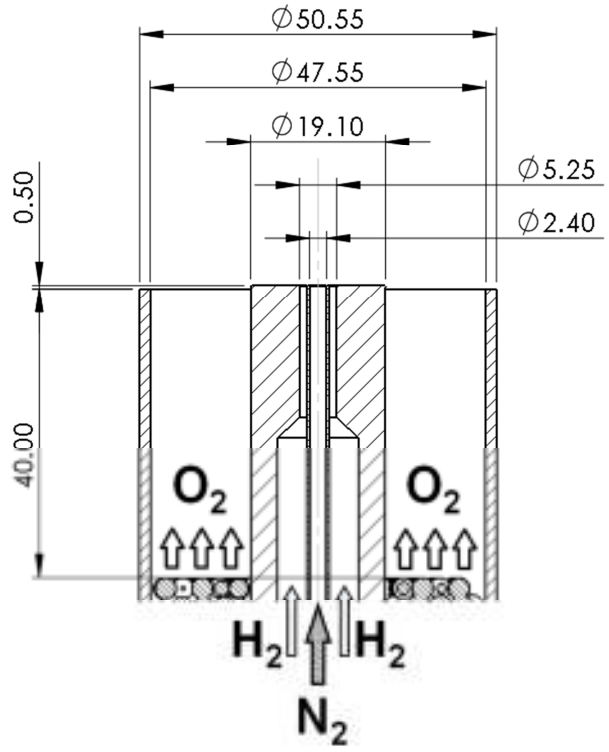

Figure 2.2 Design of the burner.

2.2.4 Materials

Commercially available powders of Al and Mg were used. Both aluminum powders were spherical, including Al 3-4.5 μm by Alfa Aesar (nominal size 3-4.5 μm) and X65 powder by Alcan-Toyo America Inc., (nominal size 6.5 μm). The magnesium powder used was 99.8% purity, -325 mesh by Alfa Aesar Stock #10233. This powder is coarser in comparison to the aluminum; particles are non-spherical but generally equiaxial. Scanning Electron Microscope (SEM) images for all three powders are shown in Figure 2.3. Compared to X65 powder, the particle sizes appear to vary in a broader range for the Al 3-4.5 μm powder, including many agglomerated small particles.

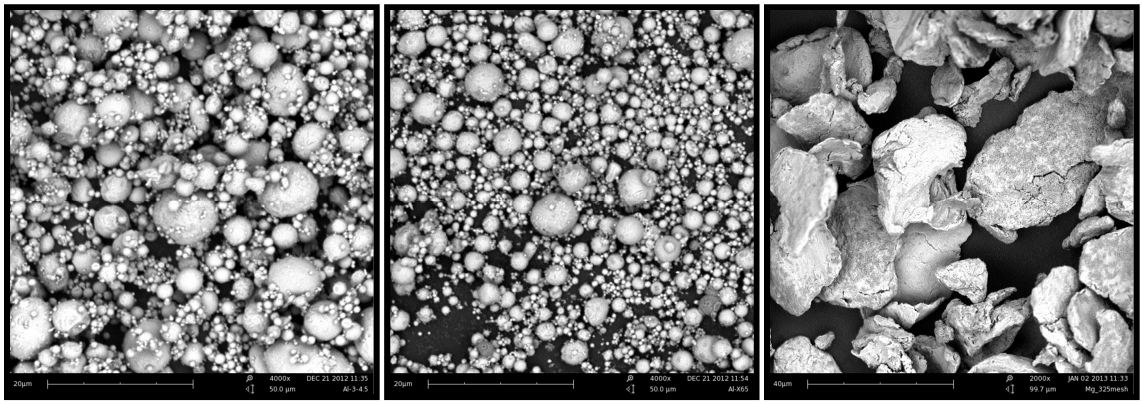

Figure 2.3 SEM images of the powders used: left to right: Al 3-4.5 µm, 20-µm scale bar; Al-X65, 20-µm scale bar; Mg -325 Mesh, 40-µm scale bar.

The particle size distributions for all three powders were measured using a Beckman–Coulter LS230 Enhanced Particle Analyzer and are shown in Figure 2.4. In agreement with the SEM image, the size distribution for the Al 3-4.5 µm includes a significant amount of small particles. The size distribution for the X65 powder is relatively narrow. The magnesium powder is substantially coarser than aluminum. As noted above, these measured particle size distributions are correlated with the burn time durations for each powder.

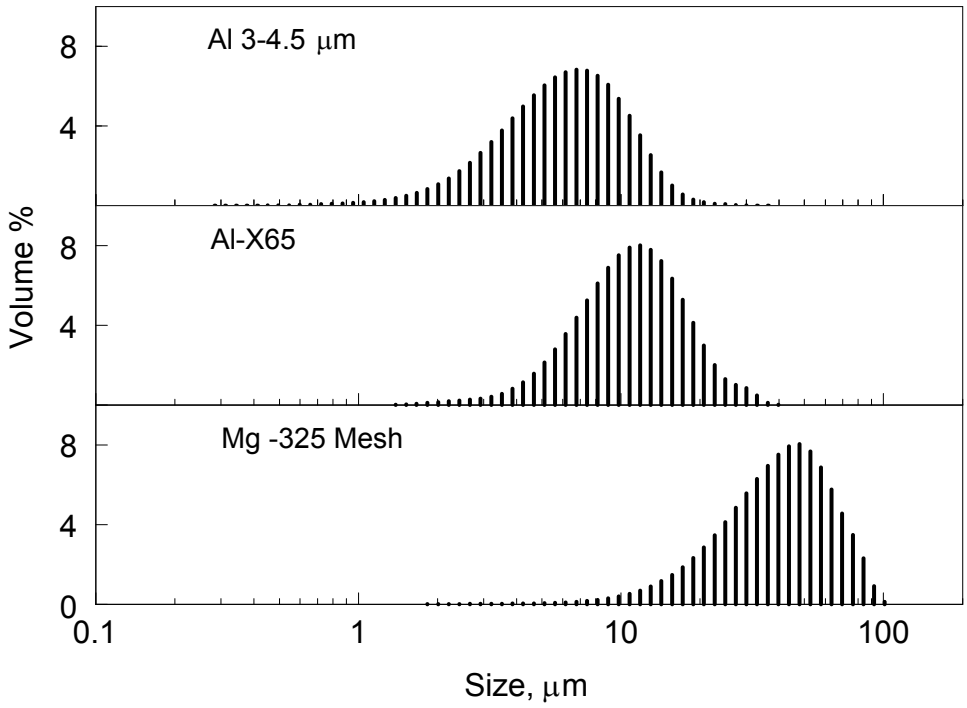

Figure 2.4 Particle size distribution for three powders used in experiments.

2.3 H_2/O_2 Flame Computational Fluid Dynamics (CFD) Simulation

The objective of the experiments was to characterize the burn rates of aluminum and magnesium particles in water. A CFD simulation was carried out to describe the gas composition, velocity, and temperature profiles within and around the produced flame, where particle combustion occurred. The model considered only the gas-phase flame with no particles following the Eulerian approach. The numerical simulation used a commercial CFD code STAR CCM+ 7.06, developed by CD-ADAPCO [56].

2.3.1 Computational Domain

The computational domain is shown in Figure 2.5 in relationship to the burner configuration. The fluid domain around the burner is described with a 2D axisymmetric mesh. The fluid domain represents an open environment that includes the burner; it is

chosen to be 150 mm along the radial direction (approximately 6 times the radius of the burner) and 500 mm from the top of the burner (about 5 times the experimental flame height). These dimensions enabled us to describe boundary regions sufficiently far from the flame and predict stable velocity profiles in the flame vicinity. An inset in Figure 2.5 shows a magnified view of the adopted mesh in the main reaction region.

The final mesh is composed by 140,000 polyhedral elements characterized by dimensions that span from 1.0 mm close to the outlet boundaries (far from the flame region) to 0.03 mm in the flame region. The grid refinement is carried out using different volume shapes enabling one to obtain a smooth grading of the cell dimension [56].

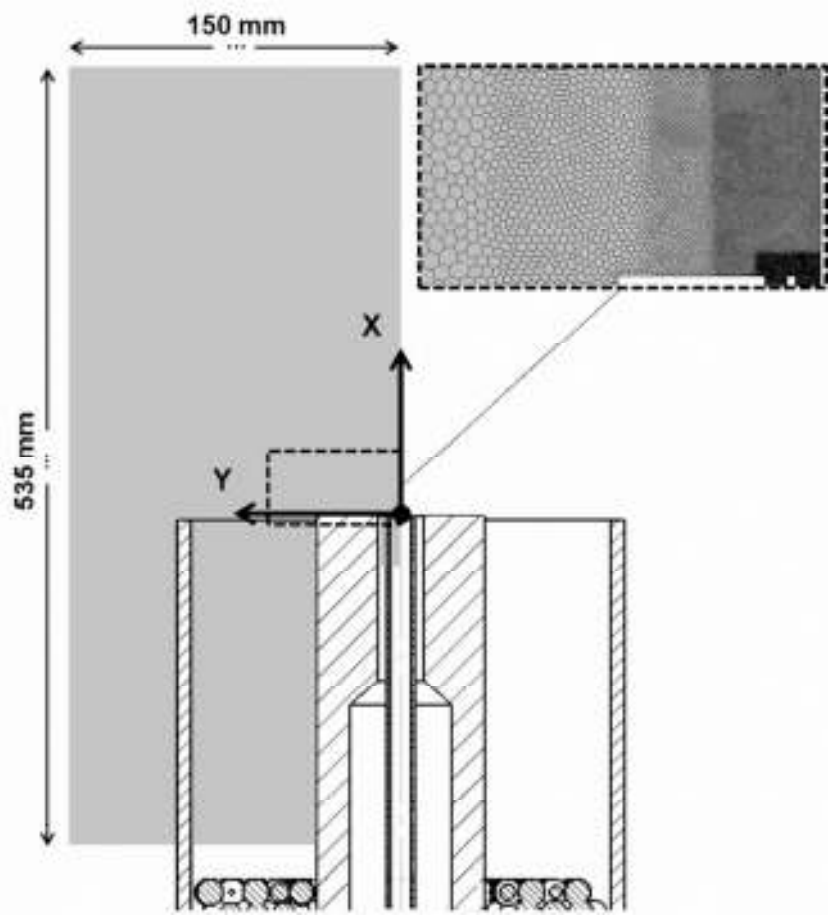

Figure 2.5 Computational domain for CFD modeling.

2.3.2 Modeling

The H_2/O_2 flame was described using a reaction model based on the adiabatic equilibrium presumed probability distribution function (PPDF) that is specific for non-premixed combustion (assuming that the reaction kinetics is fast compared to transport processes). In the adiabatic PPDF model, the atomic concentrations and the temperature determine the value of any scalar at any spatial location. Since the number of atoms in the reactor does not change because of mass conservation, the reaction state space can be characterized by a single conserved scalar: the mixture fraction. An assumption of this model is that the turbulent diffusivity is much greater than the molecular diffusivity, so that the molecular diffusivity was considered negligible. A detailed discussion of the PPDF model is available in Refs. [57, 58]. In the reaction model, all chemical species involved in the hydrogen combustion were accounted for: H, H_2, H_2O, HO_2, H_2O_2, O, OH, and O_2. The properties of species were calculated using NASA polynomials [59].

To approach the problem, a multi component ideal gas model was selected. Due to the low flame emissivity, the flame radiation heat losses were neglected, and the burner walls were considered adiabatic. The effect of gravity is accounted for. The gas mixture dynamic viscosity, μ, was calculated using the Sutherland's law (air as a reference gas):

$$\frac{\mu}{\mu_0} = \left(\frac{T}{T_0}\right)^{3/2} \left(\frac{T_0 + S}{T + S}\right) \tag{2.1}$$

where T_0 = 273.15 K is a reference temperature, μ_0 = 1.716e-5 Pa·s is the air viscosity at T_0, and S =111 K, is the Sutherland temperature [60].

The simulations were carried out under steady state conditions. The turbulence effects were modeled using the Reynolds-Averaged Navier–Stokes k-omega shear stress transport turbulence approach [61]. Attention was paid when constructing the mesh to obtain the correct values for the non-dimensional wall distance for a wall-bounded flow, y+, corresponding to the turbulence model selected.

2.3.3 Boundary Conditions

The air surrounding the burner was modeled as an ideal gas mixture composed by 76.7 mass % of N_2 and 23.3 mass % of O_2. The oxygen flow was defined by introducing a boundary condition with a constant gas velocity at the bottom of the computational domain (Figure 2.5). The flows of hydrogen and nitrogen were defined at the respective burner outlets, cf. Figures 2.2 and 2.5. Further details on the boundary conditions set according to the experimental flow rates are given in Table 2.1.

Table 2.1 Boundary Conditions

Gas	Temperature, K	Flow rate, l/min	Velocity, m/s
N_2	293.15	1.45	5.33
O_2	293.15	5.77	0.065
H_2	293.15	4.27	5.23

In all simulations, the convergence was achieved when residuals stabilized at values below 10^{-4} for each independent variable. The convergent velocity and temperature profiles were additionally inspected to identify any unusual patterns.

A qualitative comparison of the flame shape and the predicted concentration field of H_2O are shown in Figure 2.6. The general flame shape and dimensions are reproduced reasonably well. More quantitative validations of the present model are discussed below.

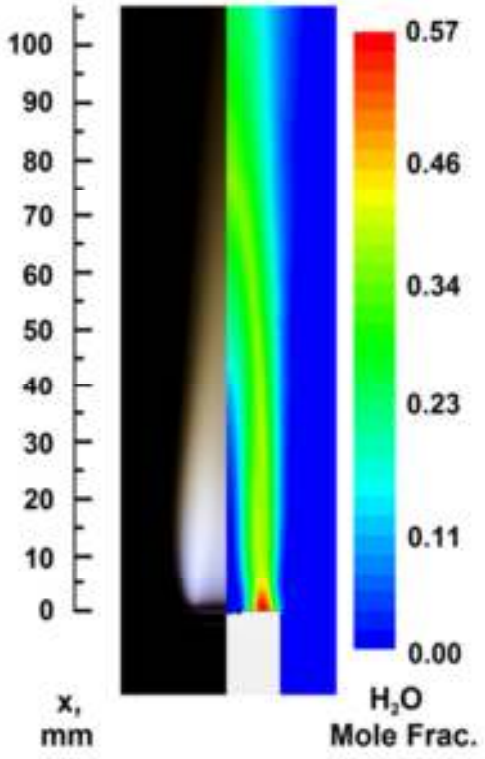

Figure 2.6. A photograph of the H_2/O_2 flame (left) and a CFD-predicted water mole fraction contour plot.

2.3.4 Validation of the CFD Results

The CFD results were validated using two different experiments. The first experiment measured the temperature profile within the flame. The second experiment quantified the gas velocity in a selected flame region.

To measure the flame temperature profile, a thin ceramic filament was inserted into the flame (with no powder fed into it), and its emission was measured using an EPP2000 High Resolution Spectrometer by StellarNet Inc. Prior to inserting the filament into the flame, the spectrum from the flame emission was recorded and treated as the baseline signal. The filament inserted into the flame was allowed to equilibrate before its emission spectrum was acquired. The measurements were performed at several filament heights, until the filament emission became weak and comparable to the background flame emission. Each recorded spectrum was approximated by a gray body emission spectrum using the emitter's temperature as an adjustable parameter. As a result, the vertical temperature profile was obtained. Because the hottest part of the heated filament produced the strongest emission signal, the measured values represent the maximum flame temperatures achieved at each height. These values were compared to the maximum temperatures predicted to exist at each height in the CFD model. The comparison is shown in Figure 2.7. The experimental and computed temperature profiles are consistent with each other. Both the plateau and the decay of the temperature at increased heights are predicted well.

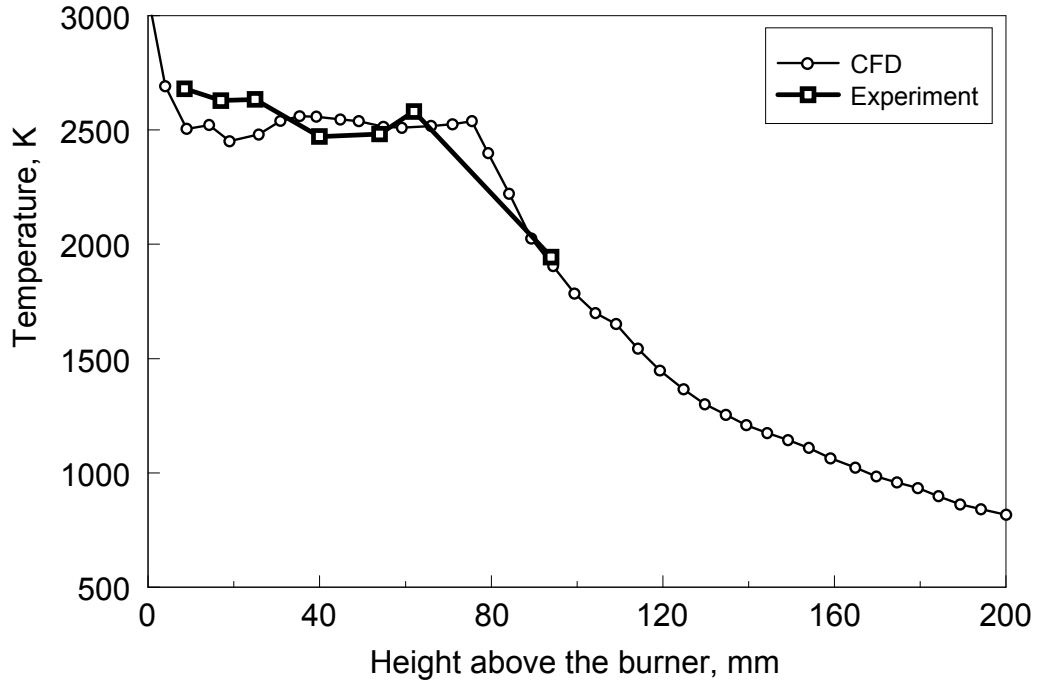

Figure 2.7 Maximum temperature in the H_2/O_2 flame as a function of height above the burner.

The gas velocity was measured using particle image velocimetry. A vertical, 532-nm laser sheet modulated with a frequency of 7500 Hz was placed at the flame. Streaks of aluminum-X65 particles injected into the flame and illuminated by the laser sheet were photographed. A 532-nm interference filter was placed in front of the camera lens to minimize the effect of the particle thermal emission. The dashed particle streaks were processed to recover the vertical components of their velocities. The results of measurements are shown in Figure 2.8 along with the predicted velocity profiles. For most particles, their vertical velocity components agree well with the predictions. Some of the particles, however, are observed to move significantly faster, which is attributed to the effect of aluminum combustion, well known to be associated with acceleration of the burning particles.

In summary, both temperature and velocity measurements correlate well with the predictions of the present CFD model. Therefore, the CFD model-predicted concentration profiles are also likely to represent well the actual environments existing in the present experiments.

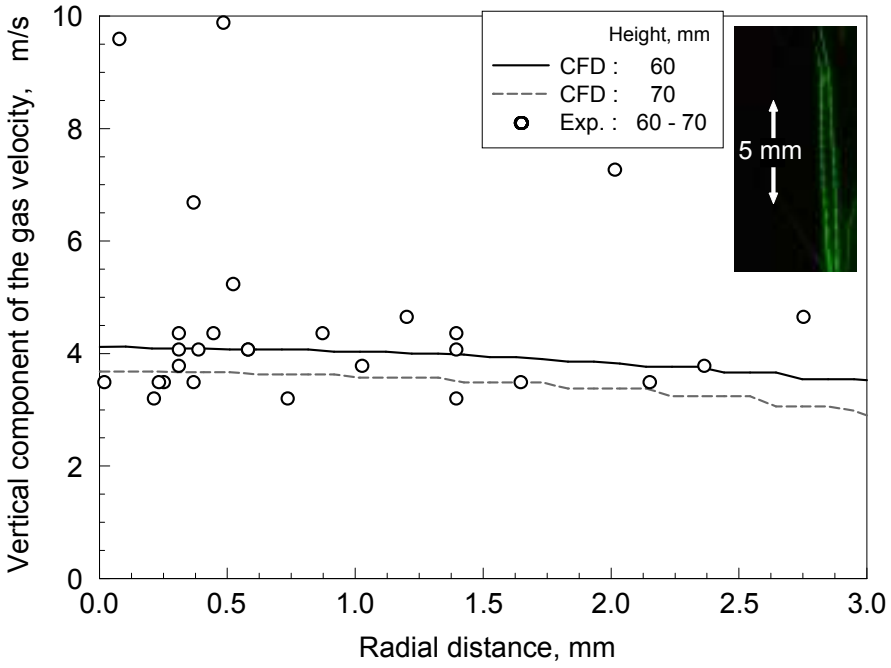

Figure 2.8 Vertical component of the gas velocity as a function of the radial distance for locations 60-70 mm above the burner.

2.4 Predicted Temperature, Concentration, and Velocity Profiles

The CFD simulation results are shown in terms of temperature, velocity, and molar distributions of species involved in the reaction.

Vertical temperature profiles and concentration profiles for the main oxidizers present in the flame, H_2O and O_2, are shown in Figure 2.9 for different radial positions. Near the burner, the temperature is high at the radial distances of about 4-8 mm, quickly

dropping further away from the burner's axis. For smaller radial distances, the temperature exceeds 1500 K approximately 40 mm above the burner.

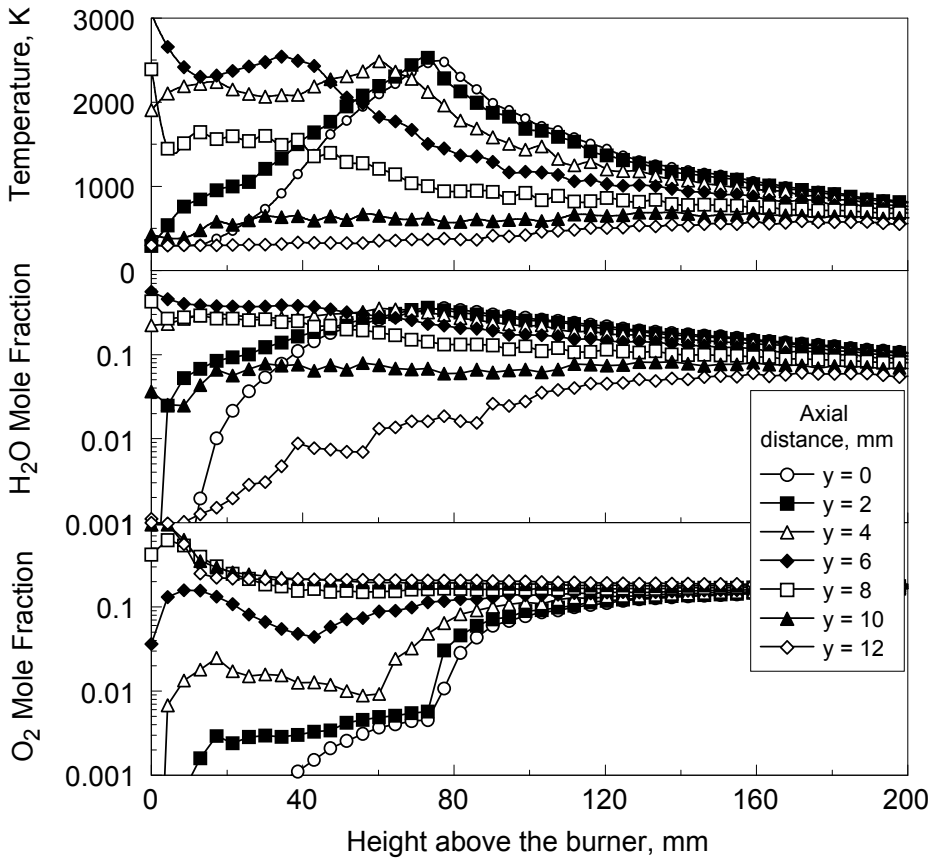

Figure 2.9 Vertical profiles of temperature and main oxidizing species at different axial distances.

The water concentration is around 30 % right above the burner at the radial distances of 4-6 mm. Closer to the center of the flame, the water concentration exceeds 10-15 % at about 40 mm above the burner. At the radial distances less than 8 mm, the water concentration remains above 20% up to about 100-110 mm above the burner. Oxygen concentrations are high right above the burner at the radial distances exceeding 8 mm. Close to the center, with axial distances less than 4 mm, the oxygen concentration

remains below 1-1.5 % up to 60 mm above the burner. Thus, the effect of oxygen as an oxidizer can be neglected for particles burning within 4 mm radius around the burner axis and consumed at the heights lower than 60 mm from the top of the burner.

Vertical profiles for mole fractions of all species produced in the H_2/O_2 flame along the burner's axis are shown in Figure 2.10. In addition to illustrating once again that the water concentration is substantially higher than that of oxygen in the region where the particles are expected to burn, the plots also show that presence of other potential oxidizers, such as O and OH, can be neglected.

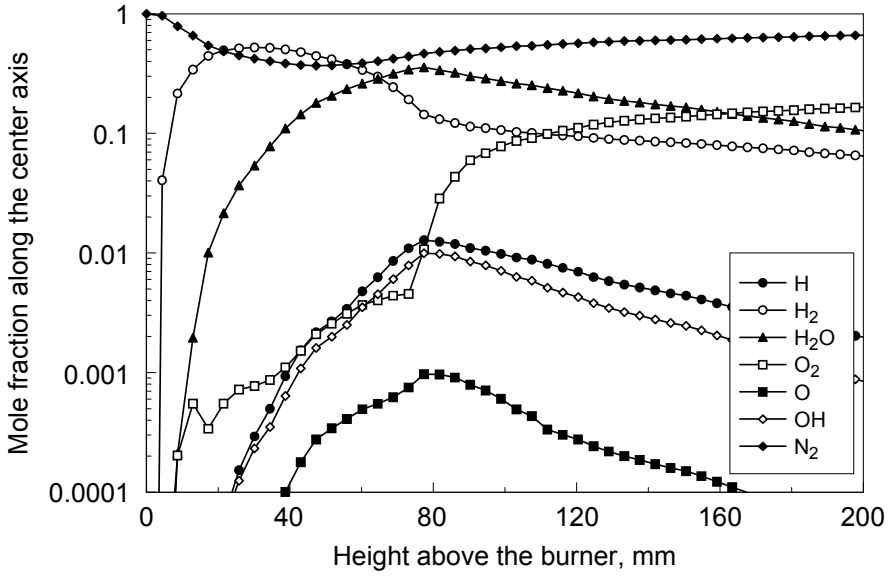

Figure 2.10 Vertical profiles of the species produced in the H_2/O_2 flame along the burner's axis.

Vertical profiles for the vertical and horizontal components of the gas velocity are shown in Figure 2.11. In the flame region, the vertical velocity component is about an order of magnitude greater than its horizontal component. However, the horizontal velocity component is not entirely negligible. It may cause some "focusing" of the particle jet in the region between 4 and 6 mm from the flame axis, as a result of the flows

of oxygen and hydrogen towards the flame sheet. This effect was, indeed observed from close inspection of the particle trajectories. However, such effects are predicted to occur (and were observed) in a relatively narrow range of heights; for the most part, the particle trajectories are defined by the vertical component of the gas velocity.

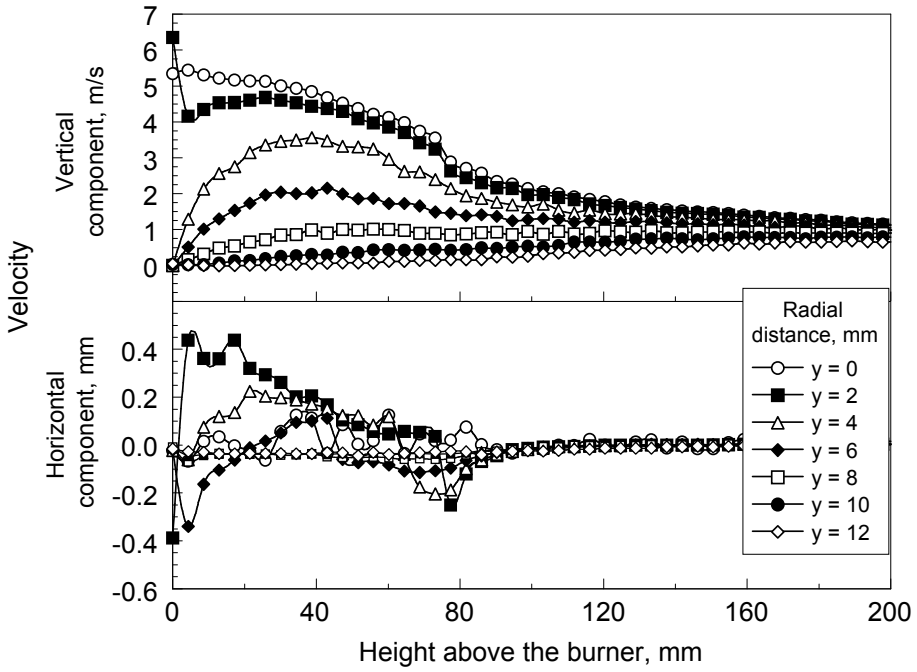

Figure 2.11 Vertical profiles for the vertical and horizontal components of the gas velocity above the burner for different radial positions.

2.5 Experimental Results

Multiple images of the ignited particle streaks were taken and processed to identify locations where they ignited and burned. An example of a characteristic photograph used in the processing as well as locations of particle ignition recovered from multiple similar images are shown in Figure 2.12. The scales for both parts of Figure 2.12 are the same, so that the particle ignition locations can be readily visualized relative to the flame region. Most particles ignite at the heights from 30 to 60 mm from the top of the burner and

within ±4 mm from its axis. Some particles ignite lower and higher than this region, very few particles are observed to ignite at the axial distances greater than 5 mm. Comparing these results with the data shown in Figure 2.9, it is clear that most particles ignite and burn in water with negligible effect of oxygen on their burn rates.

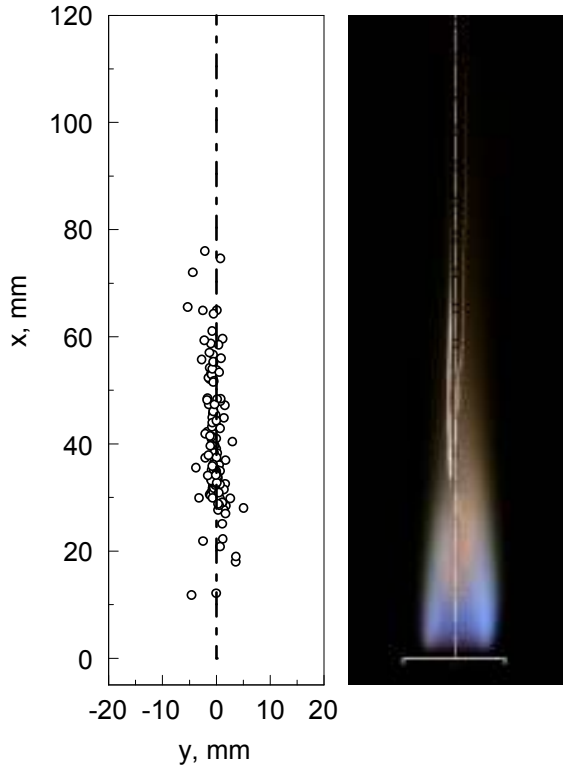

Figure 2.12 Locations of particle ignition identified from processing selected flame images (height above the burner is x and axial position is y). A characteristic flame image used in the analysis is shown on the right. The scales are the same for both the image and plot.

Particle emission was measured with a substantial background emission produced by the flame. Recorded traces were processed to select peaks with sharp rise and clear decline back to the baseline level. Particle emission peaks were also observed to have characteristic shapes separating them from the flame emission fluctuations. Characteristic particle peaks are shown in Figure 2.13 for all three powders tested. The peaks for 3-4.5 μm aluminum powder were relatively weak, so that the signal to noise

ratio was relatively low. Aluminum-X65 powder typically produced clean, strong peaks with well-distinguished patterns corresponding to different combustion stages. An initial increase in the signal emission was accompanied by an oscillatory pattern, as shown in Figure 2.13. The signal then declined and stabilized at a lower level before extinguishing, while oscillations in emission intensity continued. Qualitatively, such emission traces are similar to those observed for aluminum burning in different environments earlier [32, 33]. For magnesium, emission peaks typically showed a sharp increase in intensity followed by gradual decline. To measure burn times, the signals were processed for more than 250 individual particle peaks for each powder. The burn times were determined by the duration the signal stayed above the background flame emission level.

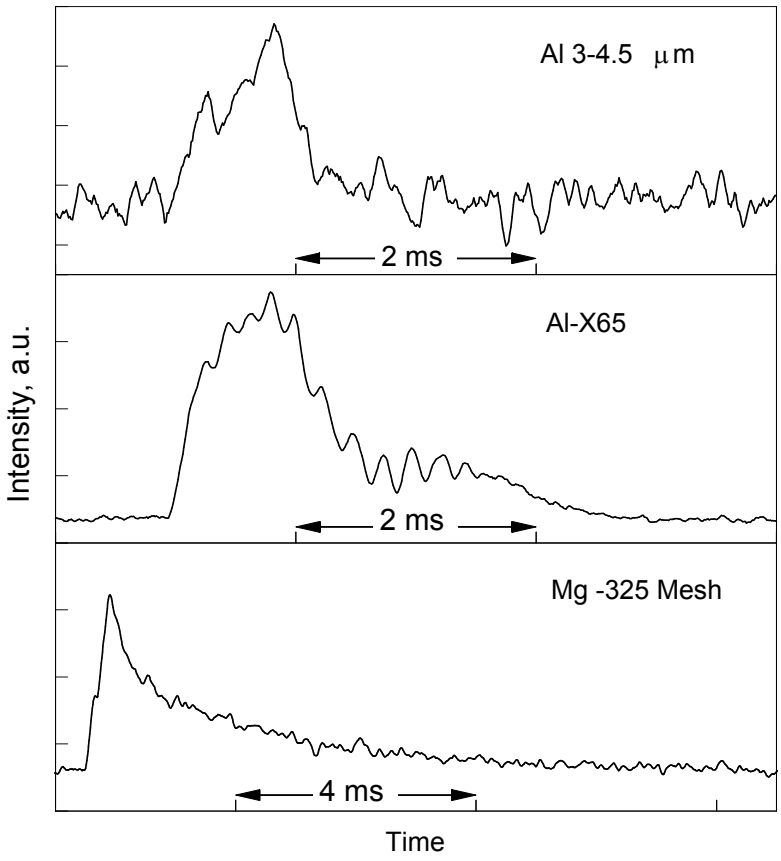

Figure 2.13 Typical particle emission peaks for aluminum 3-4.5 μm, aluminum-X65, and magnesium -325 mesh.

Recorded signals were sufficiently strong to roughly evaluate color temperatures for aluminum-X65 and magnesium powders. Traces recorded at 532 and 589 nm were used. Resulting temperatures varied in broad ranges, probably illustrating that stronger signals were needed for reliable measurements. Despite the large variation, it could be concluded that the peak flame temperatures for the aluminum-X65 and for magnesium were respectively close to 2600 and 2300 K.

The burn times measured from individual particle peaks were sorted into logarithmic bins and graphed as a histogram plotting the number of particles in each time bin. The results are shown in Figure 2.14. It was assumed that larger size particles burn

longer, so there is a direct correlation between the particle size distributions shown in Figure 1.4 (cast in terms of particle number density) and burn times shown in Figure 2.14. To justify this approach, an additional correlation, between particle burn times and emission intensities was also considered. It was expected that larger particles, characterized by longer burn times, would also produce higher amplitude emission pulses. As shown in Figure 2.15, this assumption works for most particles. Removal of a few outliers from the trends shown in Figure 2.15 did not result in a noticeable change in the observed effect of particle size on their burn times, shown in Figure 2.16.

Details of a procedure used to correlate particle size distributions (Figure 2.4) and burn times (Figure 2.14) are discussed elsewhere [55].

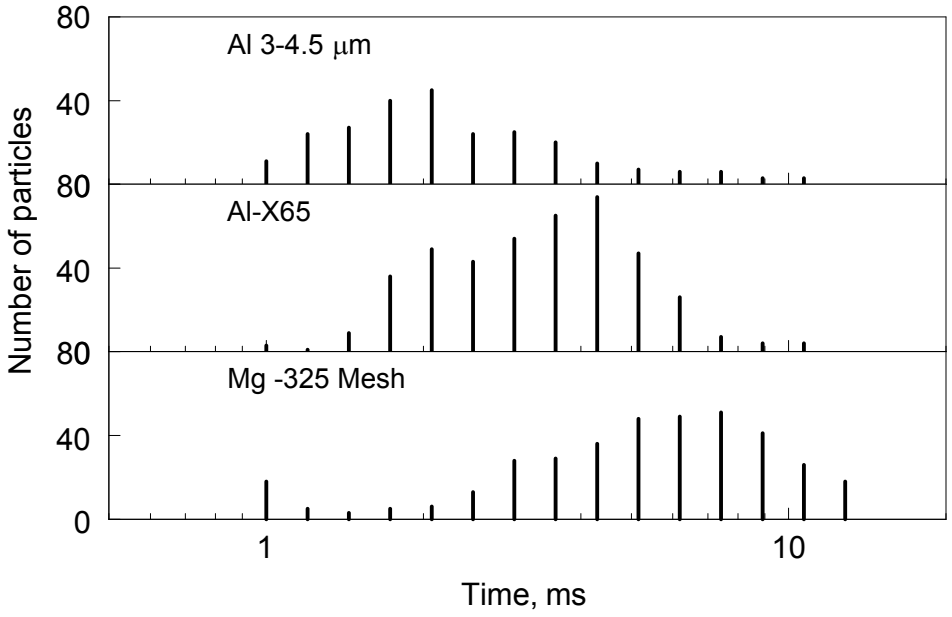

Figure 2.14 Statistical distributions of the measured burn times for different powders.

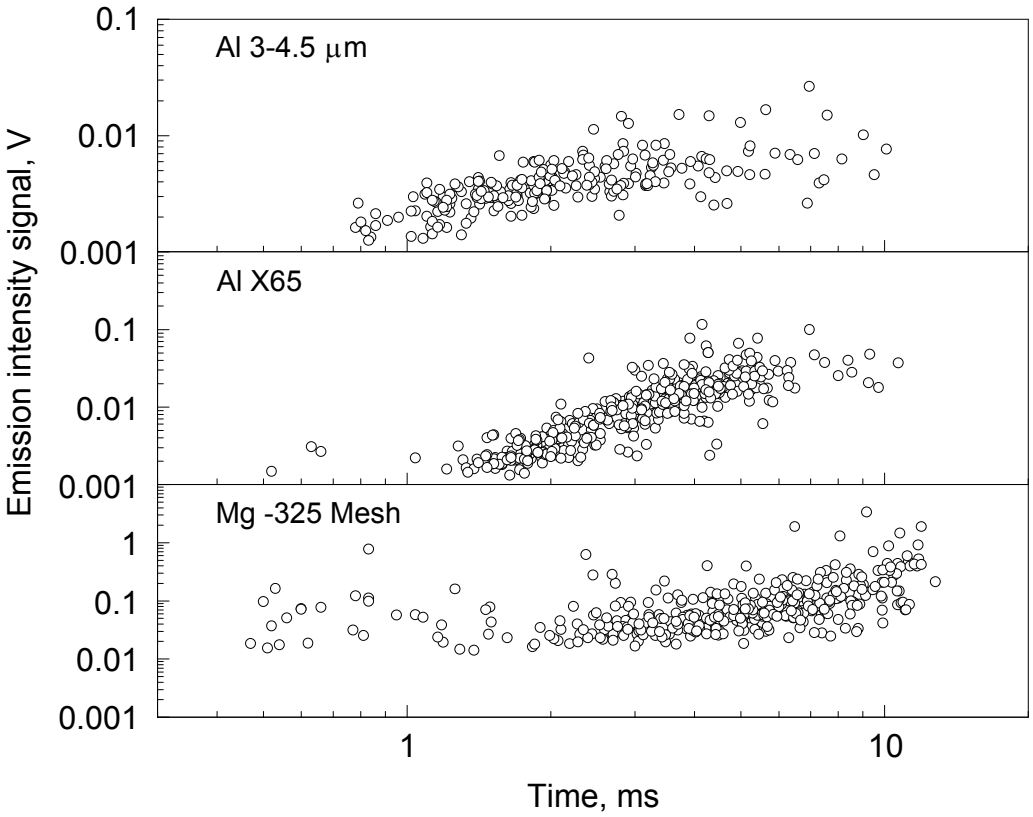

Figure 2.15 Correlations between the measured burn times and maximum emission intensities for different powders.

The burn times generally vary in the range of 1-10 ms. The effect of powder sizes on burn times is relatively weak; the straight lines shown in the log-log plot in Figure 2.17 are close to $t \sim d^{0.65}$ trends for all powders. Comparing magnesium and X65 aluminum powder, it appears that Mg particles burn somewhat longer than the same size Al.

There is a discrepancy between the trends observed for two aluminum powders. It appears that particles from the 3-4.5 μm powder have longer burn times compared to the same size particles from the X65 aluminum. These longer burn times are thought to be produced by agglomerated particles, rather than indicative of true difference in combustion rates between the two aluminum powders. Indeed, the particle size

distribution of the 3-4.5 μm powder shows a substantial presence of submicron particles; at the same time, the SEM images show that such fine particles often adhere to the larger particles, as seen in Figure 2.3. The agglomerates can be broken during particle size measurements, when the powder in solution is actively agitated by ultrasound; however, the agglomerate might survive passing through the powder feeder in the present combustion experiments. Particles in X65 aluminum have a narrower size distribution and fewer fines. Their SEM images show that they are less likely to agglomerate and skew the correlations between the measured burn time distribution and particle sizes. Based on the above consideration, further discussion of burn times for aluminum is focused only on the experimental trend obtained for X65 powder.

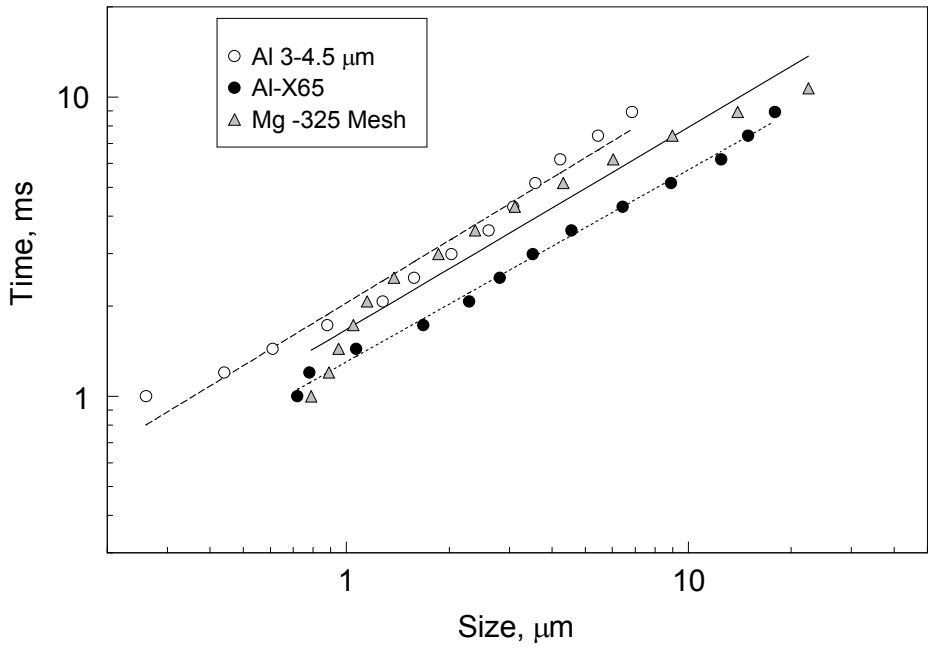

Figure 2.16 Correlations of the measured burn times and particle sizes for different powders tested.

2.6 Discussion

The results are discussed separately for magnesium and aluminum powders.

Relatively few reports identified magnesium particle burn times in water [51-53]; all such reports dealt with powders that were coarser compared to those used here. Results of the present experiments are shown in Figure 2.17 together with several data sets found in the literature. The experiments described here result in longer burn times and a weaker effect of powder size on the burn time compared to those expected for fine Mg particles based on the literature data. Using a conventional $t \sim D^n$ law, where t is the burn time and D is particle diameter, present experiments are described reasonably well when $n \approx 0.68$.

A recent study [53] used very large 1.5–5 mm particles ignited with a hot wire. Water vapor balanced with argon was supplied into the combustor chamber. Partial water pressure was 0.05 MPa. A high-speed camera was used to observe the flame structure and combustion process. The results produce a trend line described by $t \sim D^2$ relationship.

Interestingly, results from earlier experiments [51, 52] fit well with the $t \sim D^2$ trend line reported in Ref. [53]. Prachukho et al., [52], produced water vapor using a flat flame H_2/O_2 burner with an addition of nitrogen to vary the water concentration. The flame was placed in an enclosed environment. Water temperature was assessed to be about 1373 K. Magnesium particles were fed into the burner using a vibrating feeder and ignited within the flame. The particle sizes of the powder used varied between 1 and 250 μm; however, the powder was size classified into six fractions: 24-40, 37-64, 66-116, 86-133, 102-152, and 144-205 μm. Burn times were recorded on a continuously moving film and measured using a rotating disk as a shutter. Ozerov et al. [51] used the same technique for igniting

particles; experiments were performed at higher temperatures (up to 2073 K) and water concentration reaching 100%. Particles with sizes from 66 to 185 μm were used.

Surprisingly, the burn times measured for relatively coarse particles in Refs. [51, 52] are in the same range as the burn times measured in the present effort, although for substantially finer particles. The discrepancy may be explained considering that the entire length of the reaction chamber in experiments [51, 52] was less than 250 mm. It is suggested that larger particles, which burn longer simply did not have enough time to complete combustion while traveling through the chamber. This could significantly skew the measurement results. Other possible issues may relate to insufficiently well characterized oxidizing environment produced by the flat flame burner. The experimental details provided in Refs. [51, 52] are insufficient to quantify possible presence of oxygen and other oxidizers. Finally, the size classification of the 1-250 μm powder into narrow size fractions is notoriously difficult; the actual size distributions of the obtained size fractions are not reported and could have been skewed by the presence of fine particles, which are difficult to distinguish using optical microscopy.

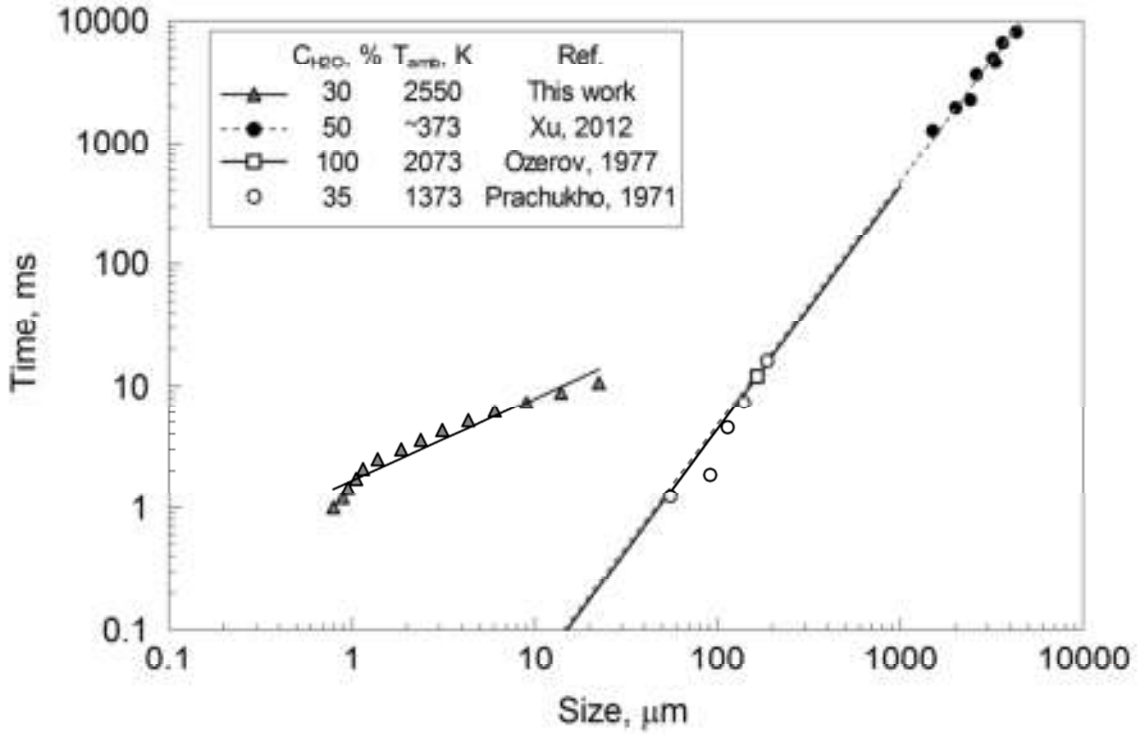

Figure 2.17 Combustion time as a function of particle size for magnesium powders [51-53].

The combustion behavior of aluminum particles in water has been studied in more details; both experimental data and empirical correlations are available to describe the respective burn rates. Present data as well as some of the earlier results and correlations are shown in Figure 2.18. The present results are reasonably well described by a $t \sim D^{0.64}$ trend.

Using the same equipment as discussed above for Mg powders, Ozerov et al., [51] investigated combustion of aluminum particles in water vapor at 2073 K at one atmosphere. Aluminum particles with the average size of 120 μm were used. Ozerov's result and proposed correlation are shown in Figure 2.18.

Recently, fine Al particles were ignited in a shock tube [31, 54]. Burn times were determined as a function of the pressure and the mole fraction of the primary oxidizers, including water, oxygen and carbon dioxide. In the reflected shock, the aerosolized aluminum particles were subjected to a high temperature (2650 K) and high pressure (8.5 atm) environment. The duration of the combustion emission pulses at 489 nm was associated with the burn times. Bazyn et al. [54] used pure spherical aluminum powders selected by sieving between 5-10 μm; the sample mass distribution showed a strong peak around 10 μm. The water mole fraction varied approximately between 0.25 and 0.55. Lynch et al. [31] analyzed two different powders: a spherical powder with the mass distribution close to 3 μm and a sample of powder selected by sieving between 5-10 μm with a mass distribution close to 11 μm. The water mole fraction varied between 0.35 and 0.65. In Figure 2.18, results of the shock tube studies are shown with large error bars accounting for the width of the size distributions for the sieved powders.

In experiments [33], that are, perhaps, most relevant to the present study, a nitrogen gas stream fed aluminum powder into a 393-K water vapor environment. The particles were ignited using a focused CO_2 laser beam. The mole fraction of water vapor produced was 0.77. The experiments used a commercial spherical powder with the nominal particle sizes of 10-14 μm and individual particle burn times were identified. The results appear to match with the present measurements for larger particles; however, the effect of particle size on the burn time is weaker and smaller particles observed in Ref. [33] to burn longer than in the present experiments. The longer burn times observed in Ref. [33] are likely associated with a much lower environment temperature.

M. Beckstead [23] proposed an empirical correlation for the aluminum particle burn times. Approximately 400 experimental data points available in literature and collected from different experiments carried out by different authors were used. These data were collected for particles with sizes spanning from 20-750 μm. This correlation defines the aluminum burning time, t [ms] as a function of the particle size, D [μm], the oxidizer mole fraction, C, the environmental pressure, p [atm], and the temperature, T [K]:

$$t_b = \frac{aD^n}{(C_{O2} + 0.6C_{H2O} + 0.22C_{CO2})p^{0.1}T^{0.2}} \tag{2.2}$$

Beckstead [23] also suggested that the data are best correlated with coefficients a = 0.00735 and n = 1.8.

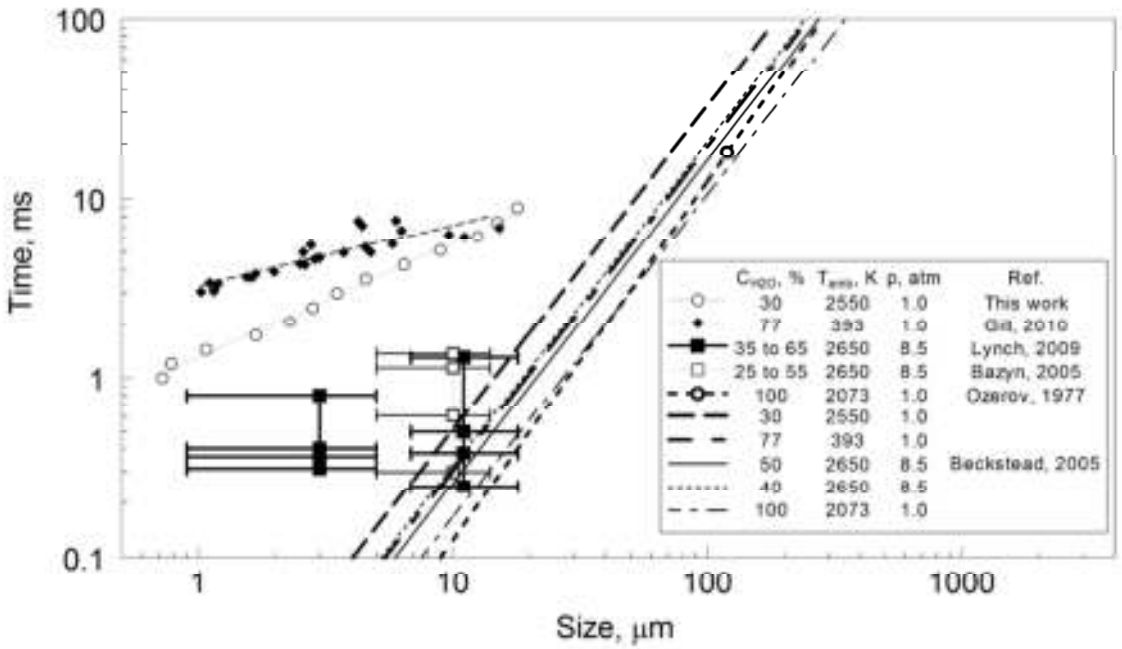

Figure 2.18 Combustion time as a function of particle size for aluminum powders (results for X65 powder for present experiments are shown) [23, 31, 33, 51, 54].

The Beckstead's correlation was used to produce trend lines shown in Figure 2.18; the experimental conditions used in all other references considered were employed, resulting in several parallel lines (for all cases, n = 1.8).

As expected, early experiments with coarse particles are well described by the Beckstead's correlation. It is difficult to make a quantitative comparison with the shock tube data, some of which seem to correlate well within the proposed trend, while others appear to deviate from it substantially. The shorter burn times reported from the shock tube studies compared to the present experiments are likely explained by the effect of elevated pressure. This effect, proposed to be very weak by the Beckstead's correlation, may become stronger for fine particles because of two reasons: the heat and mass transfer processes occur in the transition regime [62, 63] and shift in pressure results in qualitative

changes in the transport mechanisms; the pressure may also have a stronger effect for kinetically driven reactions, which are becoming more likely for fine particles [31].

The present results as well as results from Ref. [33] deviate from the Beckstead's correlation significantly. The measured burn times are about an order of magnitude longer than predicted; the effect of particle size is also much weaker than the $D^{1.8}$ trend expected based on the experiments with coarse powders. As mentioned above, changes in both transport and reaction mechanisms occurring for small particles are likely responsible for the observed combustion behavior. The weak effect of particle size on burn time observed here is consistent with our earlier experimental reports studying aluminum combustion in oxygen and other environments [32, 33, 64, 65]. A reaction model accounting for both surface reaction rates and transition transport processes is desired to interpret the present results quantitatively.

CHAPTER 3

COMBUSTION OF MECHANICALLY ALLOYED AL·MG POWDERS IN PRODUCTS OF A HYDROCARBON FLAME

3.1 Introduction

The interest in improved metal fuels is stimulated by development of solid propellants [3, 66-68], explosives [6, 14, 15, 69], and pyrotechnics [10, 13, 70]. While aluminum is by far the most widely used metal additive in energetic formulations, it was reported that advanced combustion performance can be achieved when aluminum-magnesium alloys are used [71-77]. The addition of magnesium concentration into the alloyed particles results in a lower ignition temperature for the alloy particles as compared to the pure aluminum; respectively, the ignition delays are reduced, and bulk burn rates are increased. More recently, mechanically alloyed Al·Mg powders were prepared [78-81] and were shown to burn faster in lifted laminar metal-air flames than the pure aluminum powder. However, initial comparisons of the burn rates for the laser-ignited individual particles burning in air showed that the alloy particles may burn slower than the pure aluminum [78]. Only limited information on individual particle burn rates and temperatures is available in the literature for Al·Mg alloys. Most experiments employed high pressure environments and used coarse particles [71, 72]. Very few studies systematically vary the Al/Mg ratio [72, 73, 76, 82], while most experiments [71, 74, 75, 77] and practical applications [83-90] were focused on magnalium or a common composition with the Al/Mg mass ratio of one. The oxidizing environments considered in the literature include air [91], pure oxygen [72], CO2 and N2O2 [71], and H2O [82]; however, combustion of the Al·Mg alloys in mixed oxidizers has not been considered. All

reported experiments employed quiescent or laminar gas environments, so that the effects of gas flow characteristics on the burning particle dynamics have not been studied. In most practical configurations, combustion of fine metal particles occurs in turbulent flows [29, 30, 92] and in oxidizing environments comprising mixed CO2, H2O, and other gases. This paper is aimed to characterize combustion of the micron-sized, mechanically alloyed Al·Mg powders with systematically varied Al/Mg ratio in combustion products of a hydrocarbon flame; experiments are performed in both laminar and turbulent flames.

3.2 Approach

Experiments were performed with different compositions of mechanically alloyed aluminum-magnesium powders with micron-sized particles [91]. Reference experiments were performed with a similarly sized, pure aluminum powder. Following previous work, [55], as illustrated in Figure 3.1, powder was introduced with a nitrogen jet axially into an acetylene-air flame. Particles ignited within the flame, reacting with the CO_2 and H_2O produced by the acetylene combustion. Both laminar and turbulent flames were used. The turbulence was induced by auxiliary air jets tangential to the flame. Depending on the intensity of turbulent mixing of the acetylene/air combustion products and surrounding air, burning particles could be exposed to atmospheric oxygen. Particle emission signals were captured using an array of photomultiplier tubes (PMT's) equipped with interference filters [32, 33]. The durations of individual emission pulses were interpreted as particle burn times. The distribution of burn times was acquired and correlated with the distribution of particle sizes assuming that larger particles burn longer. Particle temperatures were determined by the ratios of the PMT signals that were captured at different wavelengths.

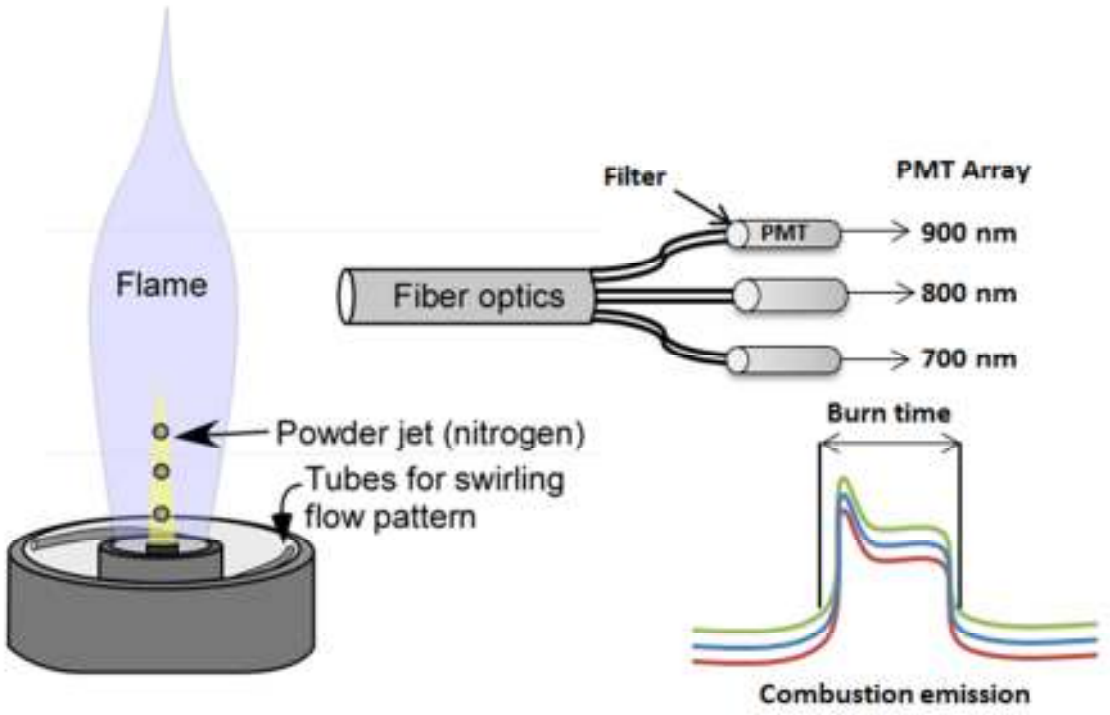

Figure 3.1 Schematic diagram of the experimental setup employing a seeded flame burner.

3.3 Experimental

3.3.1 Materials

A spherical, commercially available aluminum, X-65 powder by Alcan-Toyo America Inc., (nominal size 6.5 μm) was used. Mechanically alloyed powders with 10, 20, 30, and 53 mole % of Mg were prepared using a planetary mill and procedure discussed in detail elsewhere [78]. Scanning Electron Microscope (SEM) images for all mechanically alloyed powders are shown in Figure 3.2. The particles have characteristic roughly equiaxial shapes. The surface becomes smoother for more Al-rich samples. There is no apparent difference in the particle shapes for different alloys; all alloys range from 1-50 μm. An SEM image for the spherical aluminum used in reference experiments is shown in Figure 3.3.

Particle size distributions were measured using a Beckman–Coulter LS230 Enhanced Particle Analyzer. Preliminary measurements showed that all mechanically alloyed powders contain a small fraction of ultra-fine particles (less than 1 μm). These particles were expected to generate multiple very short emission peaks, which would be difficult to separate from the background flame emission. Small emission peaks were also expected to overlap and interfere with the peaks produced by longer burning particles. To simplify experiments, the ultrafine particles were filtered out from the powder. To filter the ultrafine particles, powder was poured in a glass vial filled with hexane. After a few seconds, most of the powder settled at the bottom of the vial and the hexane containing floating ultrafine particles was removed. This procedure was repeated 3 times before letting the final powder dry. Particle size distributions for all powders as used in experiments (after removal of the ultrafine fraction) are shown in Figure 3.4. The particle sizes all range from 1-50 μm, and a considerable overlap is shown for different powders, including spherical aluminum. Dashed vertical lines indicate the volume-based average particle sizes for each powder.

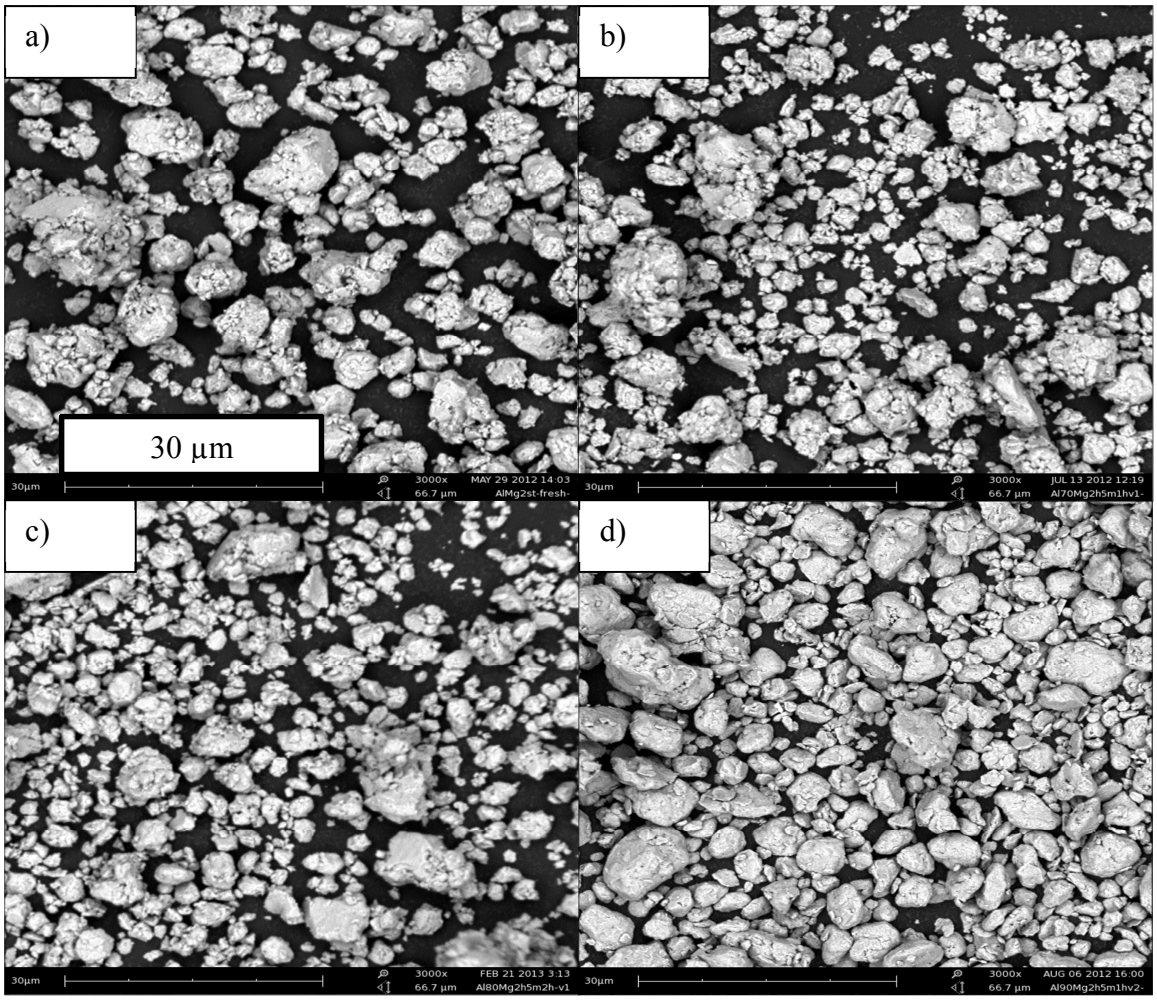

Figure 3.2 Backscattered SEM images of powders of different Al/Mg compositions; mole percent ratios: a) 47/53, b) 70/30, c) 80/20, and d) 90/10.

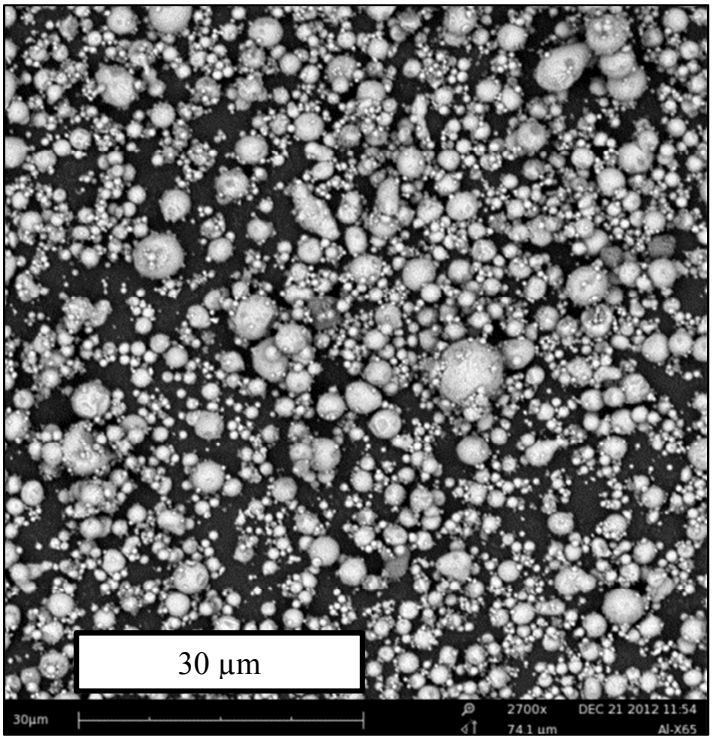

Figure 3.3 Backscattered SEM image of Al-X65 powder.

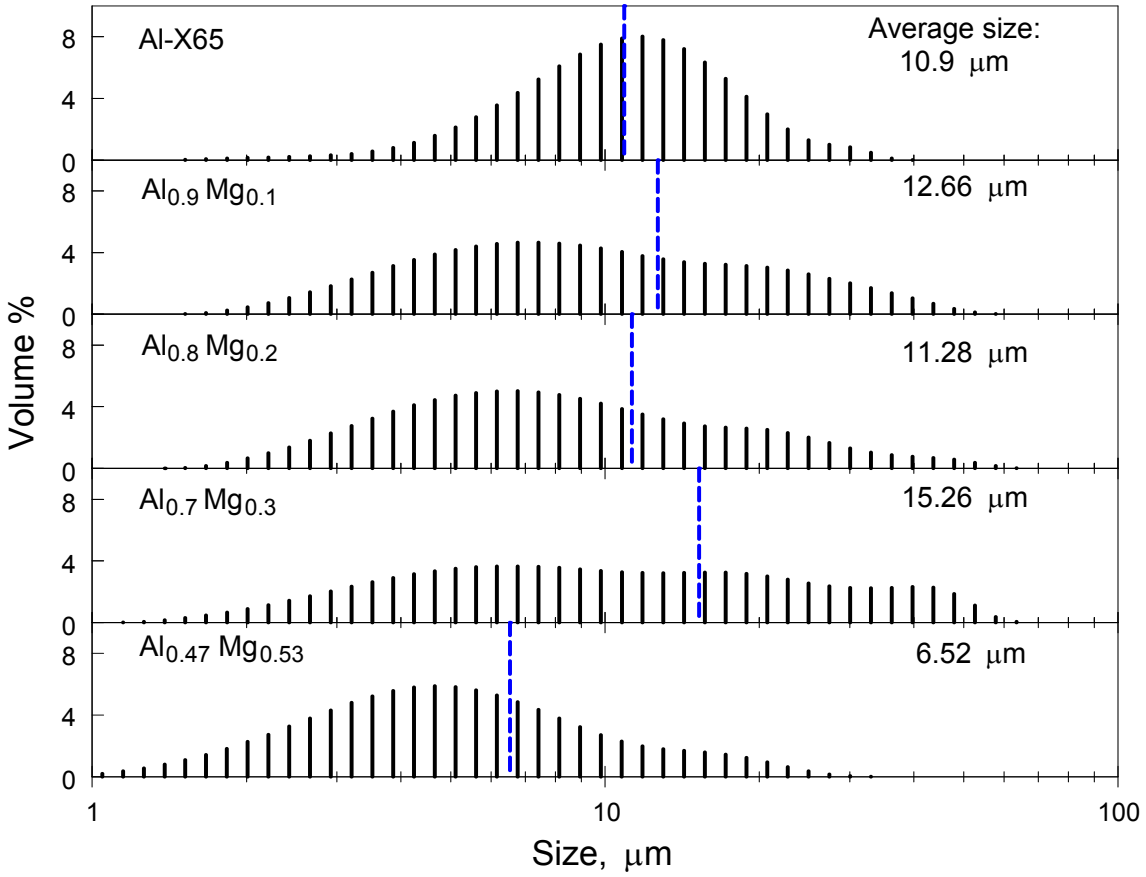

Figure 3.4 Particle size distributions for the powders used in experiments.

3.3.2 Powder Feeder

A custom screw feeder described in detail elsewhere [55, 93] was used to feed the powder into the burner. Briefly, powder was deposited in the threads of a stainless steel screw, ¾" (19.05 mm) diameter with 16 threads per inch. The loaded screw was placed into a feeder assembly, including a cylindrical brass collar and a coupling connecting it with a motor. A brass capillary tube, (1/16" or 1.59 mm OD) inserted into the collar, was used as a nozzle and crimped to conform to the screw threads. Nitrogen, fed through the nozzle, removed and aerosolized the powder from the threads as the screw rotated. The aerosol exits through an outlet in the collar connected to the burner using flexible plastic

tubing. The powder feed rate was determined by the mass of the powder loaded and the rotational speed of the screw. For these experiments, the feed rate of 0.0032 mg/s was selected to ensure production of multiple particle streaks while minimizing overlapping peaks produced by particles burning simultaneously.

3.3.3 Burner

The design of the burner generating a powder-seeded pre-mixed air/acetylene flame is described elsewhere [55, 93]. A stainless steel tube placed at the center of the burner is used to inject the particles carried by nitrogen flown at 2.0 standard cubic feet per hour (SCFH). Nitrogen flow is surrounded by a pre-mixed flow of air and acetylene fed at 10.0 and 0.9 SCFH, respectively. Turbulence is generated by an auxiliary swirling air flow, as illustrated in Figure 3.1. The auxiliary flows were produced at 50 and 70 SCFH to generate different levels of turbulence. Turbulence characteristics were estimated from the velocities and respective kinetic energies of the largest eddies in the swirling air flow, as shown in Table 3.1. Calculated Kolmogorov length scale and the Taylor microscale are shown, which can be compared to the size of individual particles and particle flames, respectively. Individual particle sizes are mostly smaller than the estimated Kolmogorov length scale, suggesting that the turbulence effects are not significant for motion of individual particles. However, the individual particle flame dimensions may be greater than the Kolmogorov length scale but smaller than the Taylor microscale, suggesting that the vapor-phase combustion processes and respective stand-off particle flames are substantially affected by the turbulent flow patterns.

Table 3.1 Characteristic Flame Turbulence

Parameter	Turbulent flow condition	
	1	2
Flow rate, SCFH	50	70
Velocity, m/s	10.4	14.6
Turbulent kinetic energy, k, m^2/s^2	54.4	106.7
Turbulence Reynolds number Re_L	23,520	32,930
Kolmogorov length scale, μm	26.3	20.5
Taylor microscale, μm	1031	871

Characteristic images of the flames produced without and with auxiliary swirling flows are shown in Figure 3.5. In all cases, the flames are seeded with the same mechanically alloyed $Al_{0.8}Mg_{0.2}$ powder. The streaks of burning particles in the laminar flame are quite long and remain close to the initial axial position, where the powder is injected. In both turbulent flames, the streaks are curving away from the flame axis and becoming shorter. It is also observed that the ending portions of some of the streaks in turbulent flames exit from the flame zone; thus respective particles finished burning in the surrounding air.

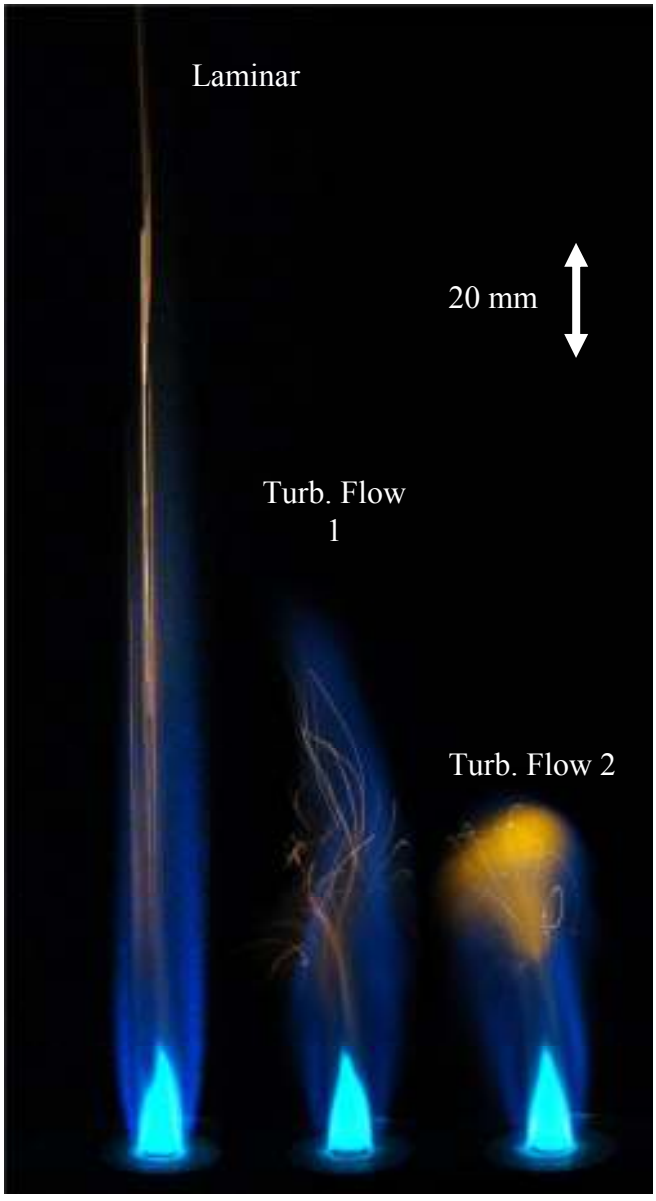

Figure 3.5 Air-acetylene flames with injected mechanically alloyed $Al_{0.8}Mg_{0.2}$ powder at different levels of turbulent mixing induced by auxiliary swirling air flows.

3.3.4 Particle Emission Intensity Measurements

A three-furcated fiber optics cable connected to three filtered PMT's was placed about 130 mm away from the central axis of the burner. Due to the effect that turbulence has on the flame height, the fiber optics was placed at 750, 350, and 300 mm above the burner for laminar flame and for turbulence conditions 1 and 2, respectively (see Table 3.1).

Each position was optimized for capturing emission from an entire particle streak while minimizing the background emission produced by the acetylene-air flame. The PMT outputs were recorded and saved at a rate of 100,000 samples per second using a 16-bit PCI-6123 data acquisition board by National Instruments and Lab-view software. The data were processed using a custom Matlab code.

3.4 Results

3.4.1 Particle Burn Times

The PMT signal includes emission from both the hydrocarbon flame and the individual burning particles. Because the flame emission intensity changes much slower than that produced by burning particles, the flame emission could be treated as a background, as illustrated in Figure 3.6. A custom Matlab code was used to process the recorded signals.

First, a baseline level was identified. A portion of the signal with at least 10,000 data points (100 ms) and with no observable particle emissions was selected. The average level of this signal was treated as the baseline level; the maximum amplitude of this signal was treated as the minimum threshold used to identify particle pulses. Every pulse above the threshold was captured. Finally, only pulses representing individual particle combustion events were selected. Pulses following one another immediately and pulses, for which the signal did not return to the baseline level, were filtered out. For selected pulses, durations were measured between the points exceeding the baseline for the rising and falling portions of the pulse.

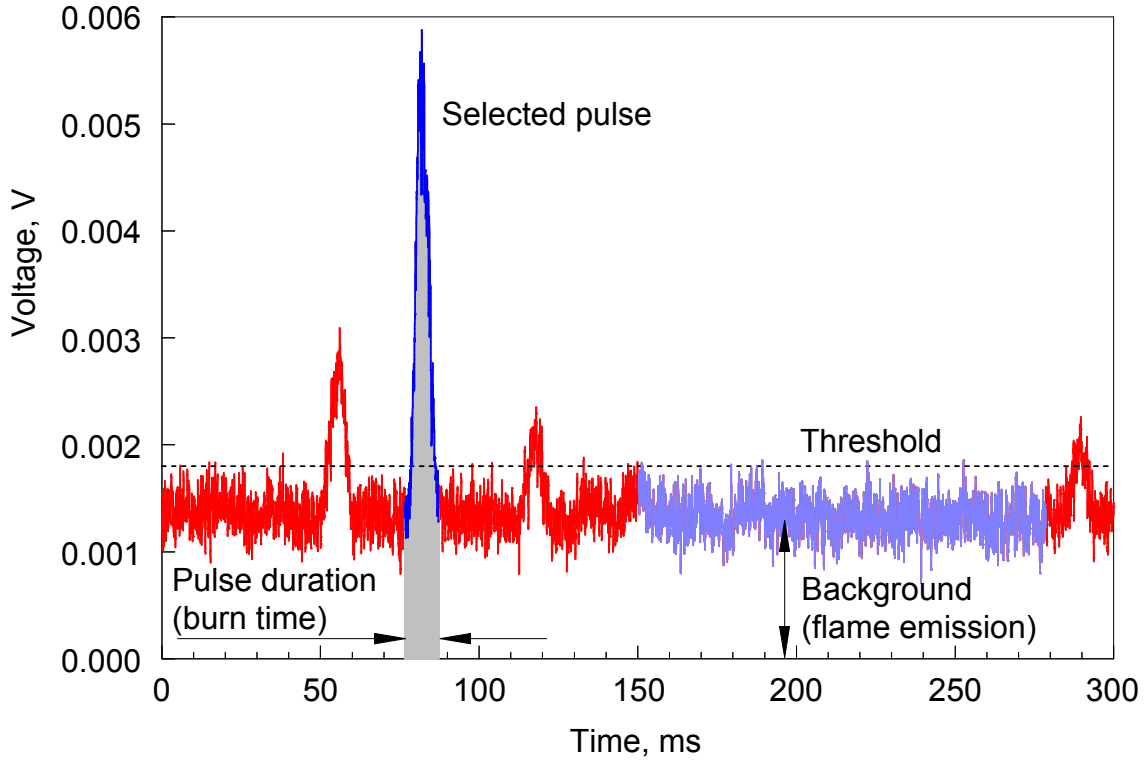

Figure 3.6 A portion of a recorded emission signal illustrating the procedure for selection of individual particle emission pulses. Data shown are for laminar flame, $Al_{0.47}Mg_{0.53}$ powder.

Characteristic particle peaks are shown in Figure 3.7 for all powders tested. As discussed below, different emission pulses could be assigned to specific particle sizes and all pulses shown in Figure 3.7 are for the particles of approximately 4.4 μm diameter. Despite substantial noise, individual particle pulses for all powders could be readily identified. Pulse durations appear to increase with the increasing concentration of Mg. In some cases, characteristic pulse shapes including oscillatory patterns and double peaks could be observed. Oscillatory emission patterns were reported earlier for combustion of aluminum particles [32, 33, 93]. Double peaks were observed for Al/Mg alloys [75, 91], where it was suggested that the first peak can be assigned to selective burn out of Mg.

Pulse durations were interpreted as particle burn times. At least 150 individual pulses were processed for each flame configuration and for each powder composition. The burn times were sorted into logarithmically spaced bins, and histograms showing the number of particles in each time bin were obtained for each set of data. Examples of such histograms for one of the alloys are shown in Figure 3.8. It is observed that the pulse durations shift to shorter times for increased levels of turbulence. This shift was observed for all powders. Assuming that larger size particles burn longer, the distributions of the particle burn times, such as shown in Figure 3.8, could be correlated with particle size distributions shown in Figure 3.4. Additional processing details are discussed elsewhere [55, 93]. After the correlation, the final plots of burn time against particle size are produced and shown in Figure 3.9. Filled symbols show reference data for pure Al, whereas different open symbols represent alloys with different compositions. The burn times generally vary in the range of 1-20 ms. For the laminar flame, coarser particles of pure Al burn faster than all alloys. However, for particles less than 5 μm, the burn rates are the highest (and burn times are the shortest) for $Al_{0.9}Mg_{0.1}$ alloy. This alloy exhibits the shortest particle burn times for all flame configurations; although the difference in burn times for different alloys in turbulent flames is smaller, compared to the laminar flame case. The data in Figure 3.9 suggest that particles with greater concentrations of Mg burn longer for all turbulence levels.

As turbulence increases, the burn times appear to decrease; from laminar to turbulent condition, the slopes of trends shown in Figure 3.9 appear to increase, indicating a stronger effect of particle size on the burn time. The effect of the particle size on its burn time is not substantially different for different alloys.

For each material and for each flame configuration, the experimental trends shown in Figure 3.9 were fit with a power law function, $t = ad^n$, where t is burn time, d is particle diameter, and parameters a and n are shown in Table 3.2. The error bars represent standard deviations for the fit values of a and n determined with 95% confidence. For all alloys, the pre-exponent, a, decreases with an increase in the turbulence intensity. The exponent, n, in most cases increases with an increase in the turbulence intensity; it varies in the range of approximately 0.6 – 1 for all materials and conditions. For all alloys, the power, n, is smaller for the laminar flame as compared to the flames with an induced turbulence.

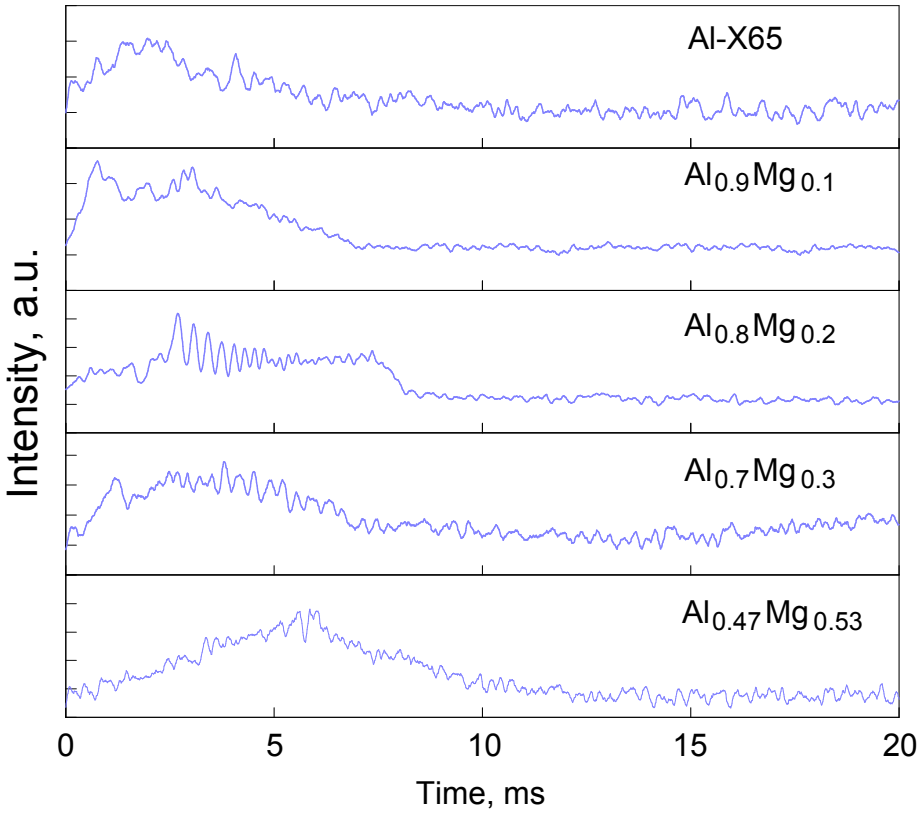

Figure 3.7 Characteristic emission pulses produced by individual particles of different materials. All particles have diameter of about 4.4 μm. Turbulent flow condition 1 (cf. Table 3.1).

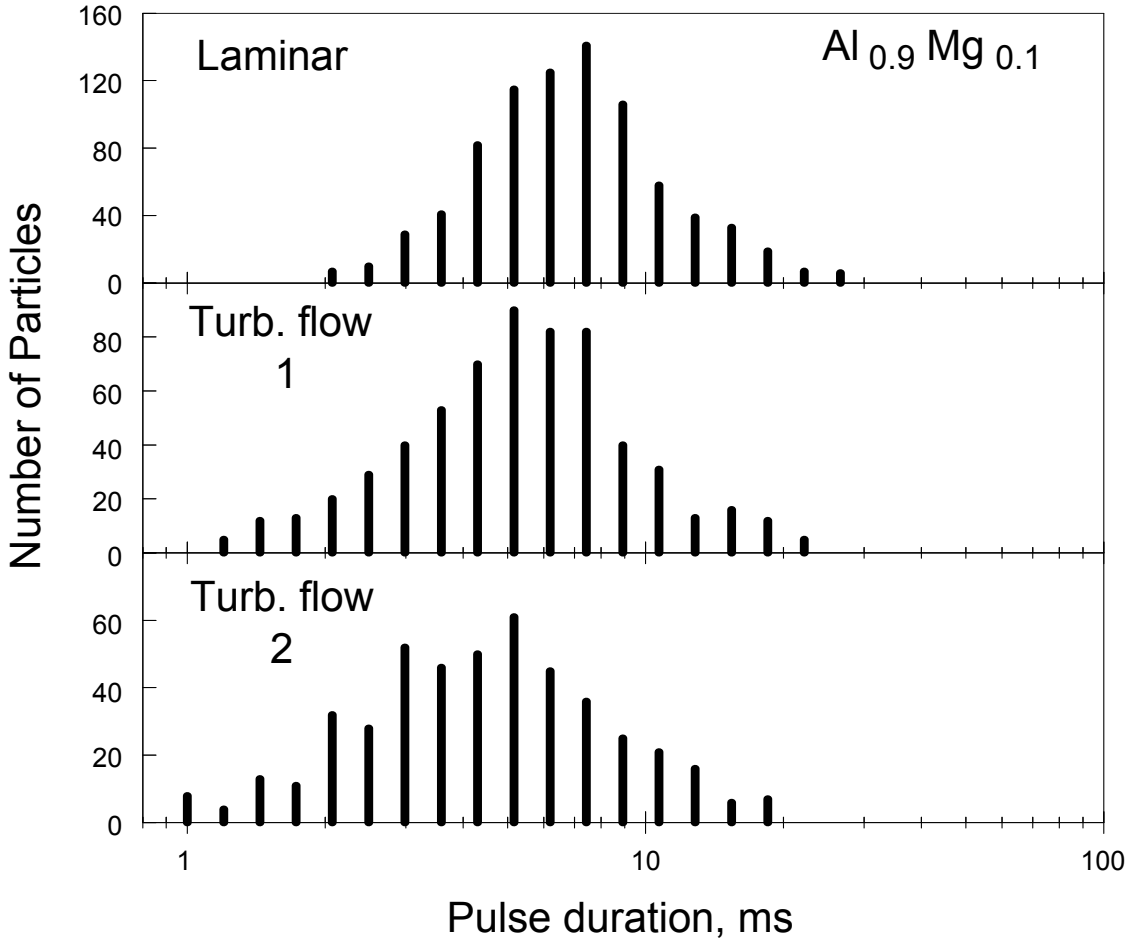

Figure 3.8 An example of pulse duration distributions for an alloy powder burning in the air-acetylene flames at different turbulence intensities.

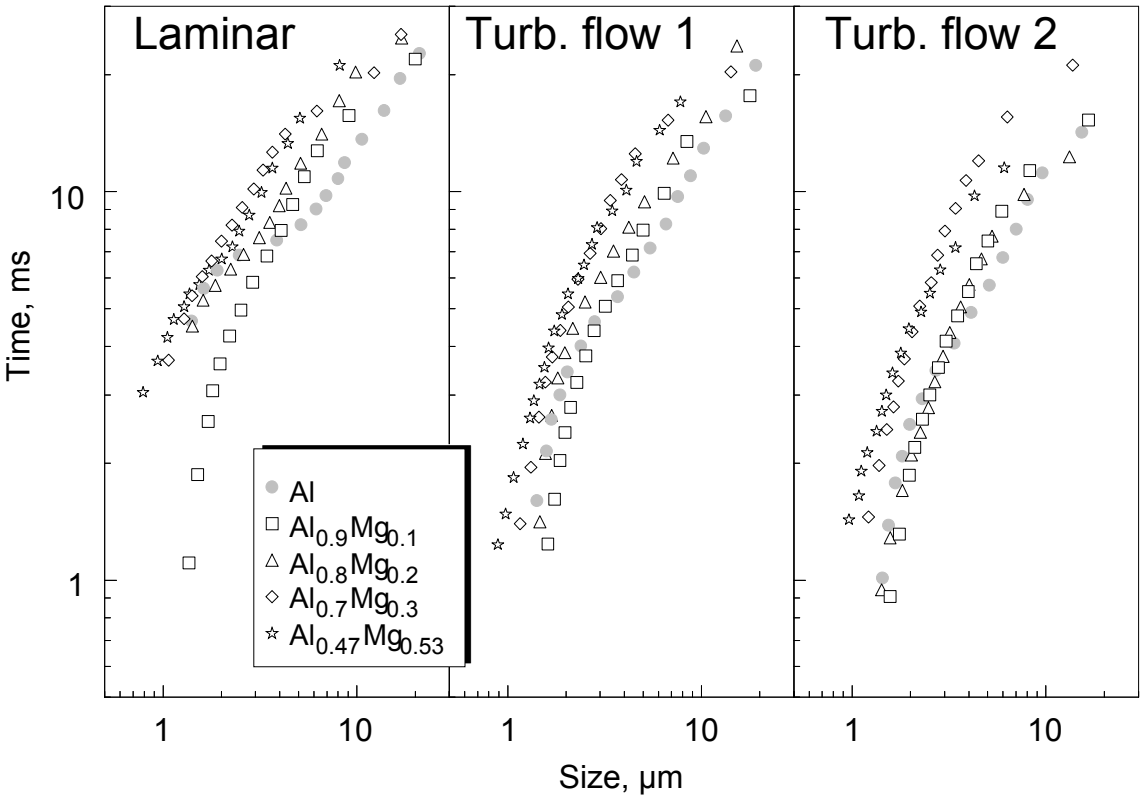

Figure 3.9 Burn times as a function of the particle size for powders of different Al·Mg alloys and pure Al burning in air-acetylene flames at different turbulence intensities.

Table 3.2 Power Law Correlation

Sample	Coefficient a ±error			Power n ±error		
	Laminar	Turb. Flow 1	Turb. Flow 2	Laminar	Turb. Flow 1	Turb. Flow 2
Al0.47Mg0.53	3.99 ±0.09	2.54 ±0.15	2.09 ±0.13	0.80 ±0.01	0.96 ±0.04	0.99 ±0.04
Al0.70Mg0.30	5.31 ±0.34	3.33 ±0.42	2.97 ±0.38	0.56 ±0.03	0.72 ±0.06	0.79 ±0.06
Al0.80Mg0.20	3.80 ±0.24	2.08 ±0.16	1.57 ±0.21	0.68 ±0.03	0.89 ±0.03	0.83 ±0.07
Al0.90Mg0.10	2.78 ±0.34	1.98 ±0.27	1.71 ±0.24	0.72 ±0.05	0.79 ±0.06	0.81 ±0.06
Al-X65	3.19 ±0.29	1.74 ±0.06	2.16 ±0.27	0.63 ±0.04	0.85 ±0.01	0.63 ±0.04

3.4.2 Particle Temperatures

Temperatures were obtained from the measured emission intensity ratios filtered at 700, 800, and 900 nm. The ratios were preliminarily calibrated using a tungsten lamp operated at different DC currents. The lamp's temperature for each current was measured by a calibrated EPP2000 High Resolution Spectrometer by StellarNet Inc. An example of the measured individual filtered emission traces and respective temperatures, implied by their ratios, is shown in Figure 3.10. The temperatures for both intensity ratios are consistent with each other when the emission signal is sufficiently strong. In this particular case, the temperature of the burning particle is close to 2500 K.

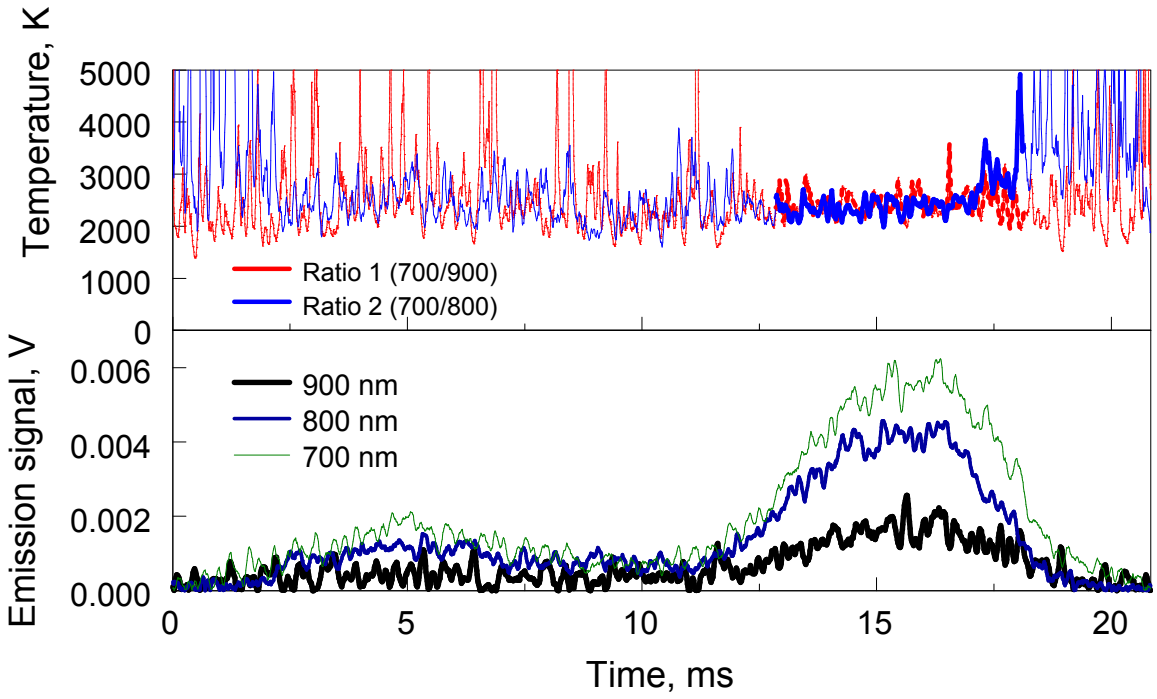

Figure 3.10 An example of a single emission pulse recorded by three different filtered photomultiplier tubes and the respective temperatures inferred by the intensity ratios. The material is $Al_{0.47}Mg_{0.53}$ alloy powder; the flame is laminar.

To process multiple emission pulses, the temperature was measured and averaged for each of the emission ratios for the time while the emission signals were above their half-peak values for each individual pulse. The correlations between temperatures obtained from different ratios were assessed considering histograms, such as shown in Figure 3.11. The example illustrated in Figure 3.11 uses $Al_{0.9}Mg_{0.1}$ powder burning at different flame configurations. Two sets of bars show distributions of the temperatures measured using different intensity ratios. Note that there are more particle peaks available for the measurement based on the 700 nm/800 nm ratio. This is because the intensity of the signal filtered at 900 nm was lower and, for some of the identified emission pulses, it was inadequate for the temperature measurement. The range of temperatures is relatively broad, from 2000 to 5000 K. The distribution shapes and peak positions are similar for both histograms for each flow condition. The peak position indicates the most likely particle temperature; it shifts slightly to higher temperatures for more turbulent flows. This trend was observed for all powders.

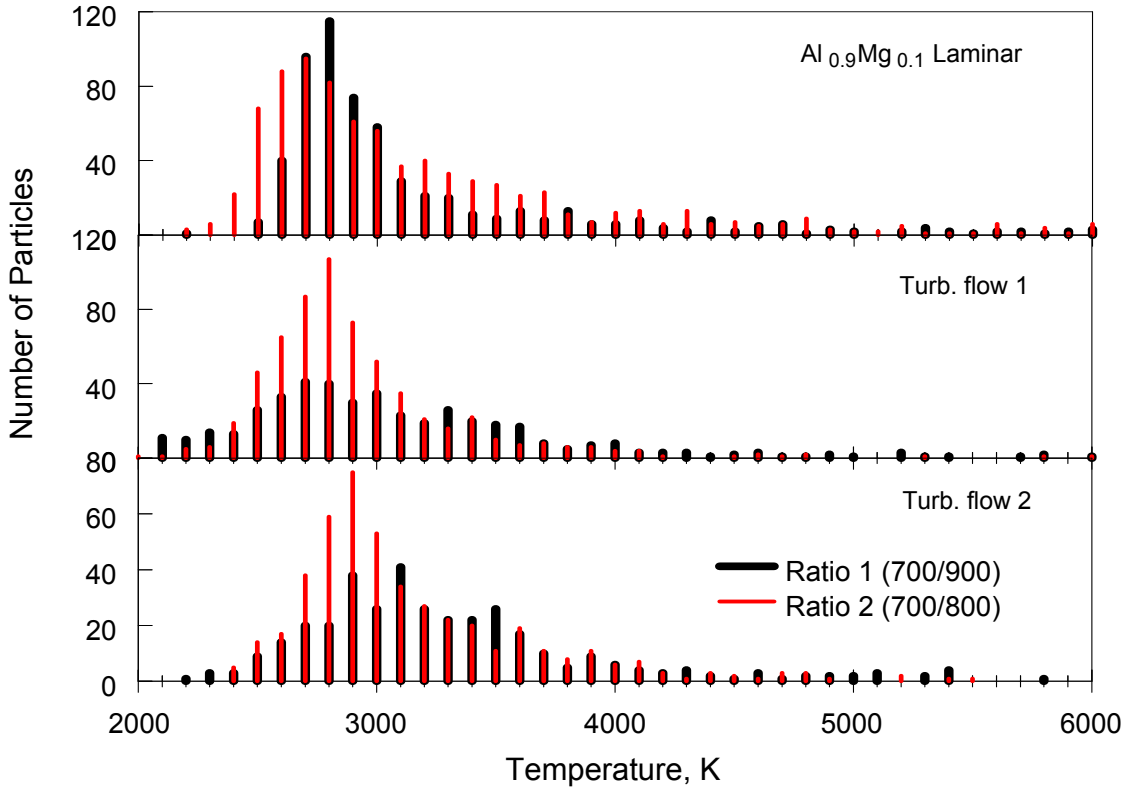

Figure 3.11 Statistical distributions of temperatures measured based on different emission intensity ratios for particles of an $Al_{0.9}Mg_{0.1}$ alloy powder burning in flames with different turbulence levels.

Results of temperature measurements are summarized in Figure 3.12, where the temperature histogram peak positions with the standard deviation shown as error bars, are presented for different alloys burning at different flow conditions. Results are shown, for clarity, for only one of the temperatures measured using the 700 nm/800 nm ratio. The temperatures between 2700 and 3000 K are observed for pure Al and for alloys with Mg concentration up to 30%. For the most Mg-rich alloy, the temperature is reduced to about 2400 K. The effect of turbulence is relatively minor, although the highest temperature is observed for the most turbulent flow for all alloys.

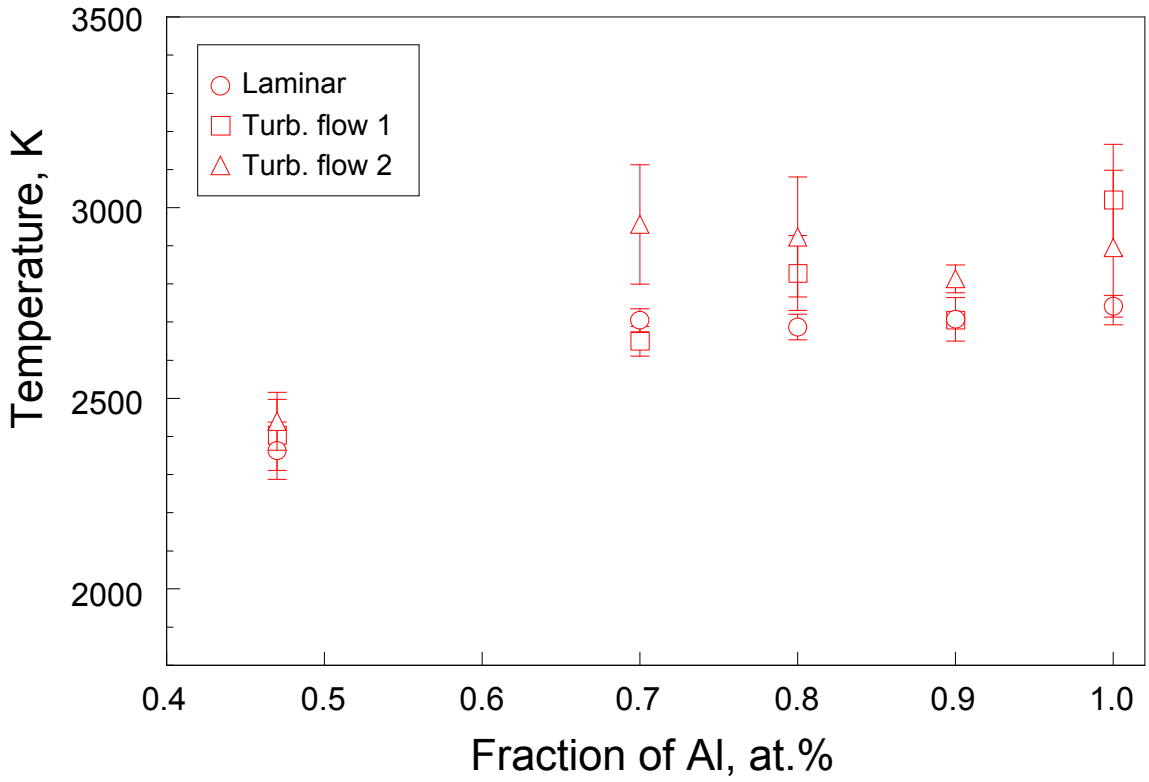

Figure 3.12 Effect of composition on the measured temperature for powders of Al·Mg alloys burning in flames with different turbulence levels.

The measured temperatures were also correlated with the particle sizes. Following the processing of pulse durations (cf. Figure 3.9), the correlation with particle sizes was established. Pulses were sorted based on their durations and thus respective implied particle sizes. Average temperatures were calculated for each particle size bin. An example of this processing for $Al_{0.9}Mg_{0.1}$ alloy is shown in Figure 3.13. No discernable effect of particle size on its temperature was observed for either of the flow conditions. This conclusion remained valid for different alloys.

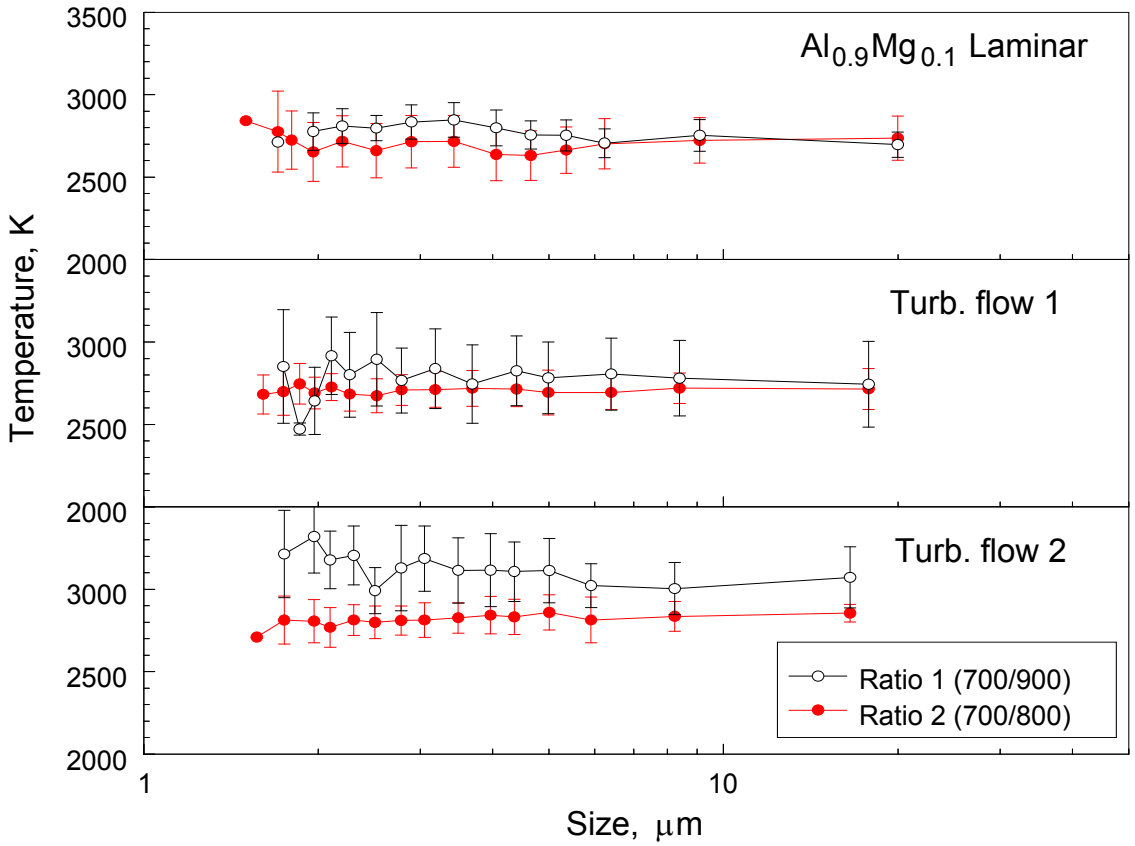

Figure 3.13 Particle temperatures for an $Al_{0.9}Mg_{0.1}$ alloy powder burning in flames with different turbulence levels as a function of the particle size.

3.5 Discussion

Effect of particle sizes on their burn times may be expressed using a power law with a relatively low exponent for all alloys, as shown in Figure 3.9 and Table 3.2. The exponent value less than one is consistent with the recent experiments with pure aluminum using the same burner and the same air/acetylene flame as in the present study [55]. Similar small values of exponents were recently reported for many small metal particles burning in different environments [32, 33, 64, 94-96]. It has been proposed that the relatively weak effect of metal particle size on its burn time is associated with the transition heat and mass transfer regime for particles with dimensions comparable to the

mean free path of the gas molecules [64, 97]. In addition, combustion regime is expected to change from vapor-phase to surface reaction for this same particle size range [94, 95].

Differences in the value of *n* for different alloys burning in the flames with the same turbulence levels are relatively small and do not show a consistent trend. For all cases, the values of *n* are greatest for $Al_{0.47}Mg_{0.53}$, and smallest for $Al_{0.7}Mg_{0.3}$ alloys. This could be interpreted as indicative of the strongest effect of vapor-phase reactions for the former composition and, respectively, the weakest effect for the latter. The strongest effect of the vapor phase reaction for the alloy with the greatest concentration of the more volatile metal, Mg, is not surprising. However, because the value of *n* does not simply scale with the Mg concentration, the changes in the burning regime as a function of the alloy composition must involve different competing processes. In one possible scenario, condensed products of Mg may be accumulating on the surface of the burning particle impeding evaporation of aluminum. This effect may be small for low concentrations of Mg (e.g., lower than 30%). Conversely, it may be compensated by evaporation of Mg for the case of very high concentration of Mg.

An observed increase in the value of *n* for the turbulent mixing compared to the laminar flames may be interpreted to suggest a greater role for the vapor phase reactions in more turbulent environments. This can be explained by stronger temperature and concentration gradients developed above the burning particle surface in turbulent flows. Such stronger gradients accelerate vapor-phase heat and mass transfer processes, leading to their greater effect on the burn rates.

The effect of alloy composition on its particle burn time is generally consistent with recent experiments, in which the same mechanically alloyed Al·Mg powders were

ignited by a CO_2 laser beam and burned in room temperature air [91]. Present results obtained with the laminar flames as well as data by Aly et al., [91] are shown in Figure 3.14. Although in both experiments the burn time vs. particle size plots may cross one another for different alloy compositions, it is apparent that the burn times are generally longer for the alloys with greater concentration of Mg. Burn times for all alloys are substantially longer for the present experiments compared to Aly et al., [91], highlighting a strong effect of oxidizer on the burn rate.

Longer burn times observed for $Al_{0.47}Mg_{0.53}$ as compared to other alloys may be associated with the lower temperature measured for this powder for all flow conditions (cf. Figure 3.12). The difference in the measured flame temperatures cannot be interpreted by different adiabatic flame temperatures of Al and Mg. Maximum adiabatic flame temperatures for both Al and Mg burning in a 2/1 mixture of CO_2 and H_2O, ideally produced by the acetylene/air flame were calculated using NASA CEA code [98]. It was assumed that 80% of the gas preheated by the air-acetylene flame to about 2000 K was comprised of nitrogen with the balance of CO_2 and H_2O. Concentrations of each metal were varied to obtain the maximum temperature. Each metal was initially taken at its melting point. Adiabatic flame temperatures are reasonably close to each other for Al and Mg; the highest temperatures for Al and Mg were close to 2940 and 2850 K, respectively. As expected, both temperatures are higher than the measured values for all alloys. The lower temperature observed for $Al_{0.47}Mg_{0.53}$ alloy may be interpreted considering a suggested above greater role of the vapor phase reactions in its combustion. Note that the temperatures inferred from the recorded emission intensity ratios are affected by the emission from both particle surface and the standoff vapor phase flame. The surface

temperature of a metal or alloy particle is limited by the boiling point of the more volatile compound. While Mg is present in the alloy, its temperature is expected to be rather low. Thus, the total emission signal produced by both particle surface (with rather high emissivity but low temperature) and by the flame (with high temperature but low emissivity), would be substantially biased to lower temperatures. However, for some compositions and for some combustion configurations, substantial amount of crystalline MgO may be condensed at and attached to the burning particle surface. Such attached MgO may become heated to a temperature substantially greater than the boiling point of Mg for the rapidly developing flames and for the flames adjacent to the particle surface. If such overheated MgO crystallites are attached to the burning particle surface, emission from such particle can become much stronger than that from an uncoated boiling metal or alloy. In addition, heat transfer to the boiling alloy/metal may be affected. Thus, the low-temperature bias caused by the difference between the flame and particle surface temperatures can be substantially reduced. For $Al_{0.47}Mg_{0.53}$ alloy, the initial rate of Mg evaporation is expected to be higher than that of other alloys, causing the Mg vapor phase flame to form further away from the particle surface. Thus, effect of surface-condensed MgO may be smaller. For this composition, therefore, the temperature measurements are substantially biased to low temperature values of the uncoated or lightly coated burning alloy. For alloys with lower Mg concentration, the vapor-phase flames form closer to the particle surface and the condensation of MgO on the particle surface is more likely. Thus, the low-temperature bias is reduced and higher temperatures are measured.

Burn times obtained here for different alloys are further compared with earlier reports by Zenin et al., [71], Roberts et al., [72], and Ozerov et al., [82] for relevant

Al·Mg alloys in Figure 3.14. Experiments by Zenin et al., [71] used much coarser alloy particles than the present work and, respectively, show substantially longer burn times. However, results by Ozerov et al. al. [82] show the burn times comparable to the present ones, although measurements were performed for coarser particles. The oxidizer was water vapor, which is expected to be more effective than the mixture of CO_2 and H_2O employed in the present experiments. Experiments used size classified particles with nominal narrow size fractions from 66 to 185 μm but, the actual size distributions of the powders used were not measured. It is, therefore, likely, that the fine particles, which are difficult to completely remove by regular sieving, were present in different size fractions and biased the measured burn times to short values. Finally, Roberts et al., [72] report data on combustion of Al·Mg alloys in pure oxygen at elevated pressures. Thus, the short burn times may be caused by this very different and effective oxidizing environment compared to the present experiments.

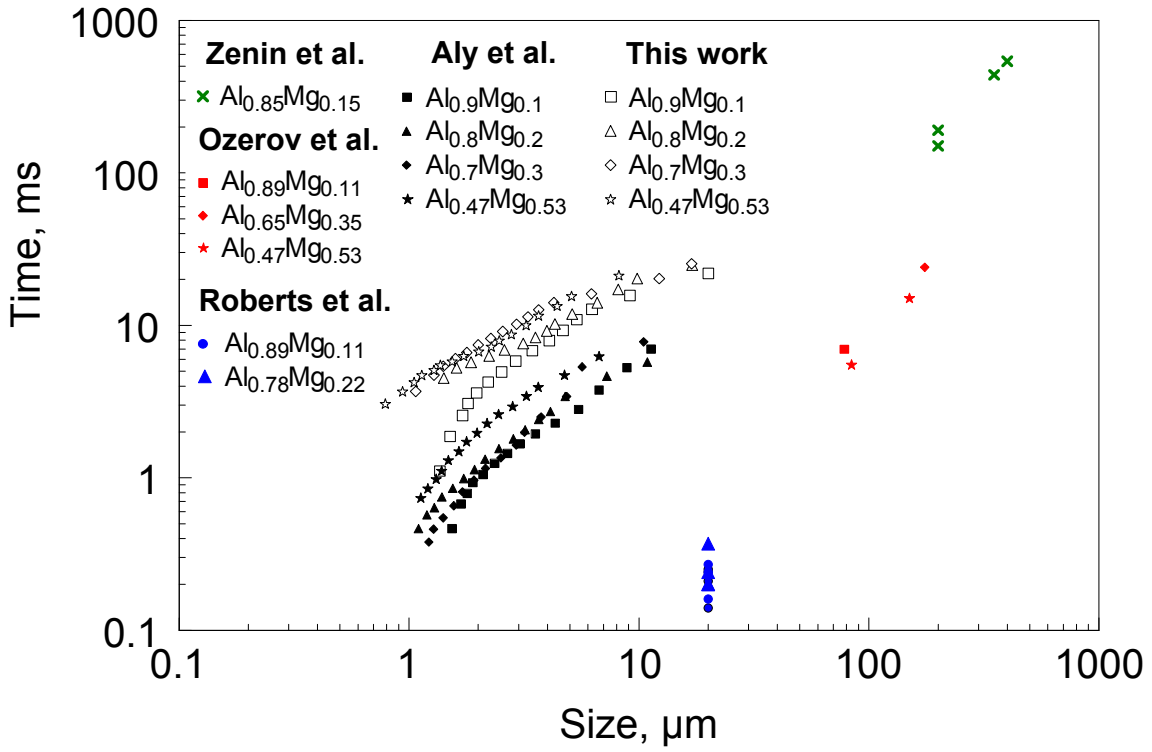

Figure 3.14 Burn time versus particle size: present results and earlier reports for Al·Mg alloys [71, 72, 82, 91].

CHAPTER 4

CONCLUSION

An experimental methodology is developed to study effect of mixed gas environments on combustion of various metal powders. In Chapter 1, experiments performed with a laminar flow and two different turbulence levels have shown a significant effect of flow conditions on the burn rates of aluminum powders. The measured burn times are longer than predicted for the micron-sized Al particles using a recent correlation based on survey of earlier experiments, mostly with coarser Al powders [23]. In agreement with recent studies [31-34], the burn times are proportional to $d^{0.3}$. Increased turbulence intensity results in substantial reduction of the particle burn time. The experimental bulk burn rates are well described by a $\sim d^{2.69}$ function for all flow conditions. Present data suggest that the burn rate for particle combustion in a laminar environment should be multiplied by $1+18.2I$, where I is turbulence intensity, to estimate the acceleration of aluminum combustion in turbulent environments similar to those considered in the present experiments.

In Chapter 2, combustion of fine magnesium and aluminum powders was characterized in a high temperature water vapor. For the selected experimental configuration, effect of other oxidizers on the measured particle burn rates could be neglected. The composition and temperature profiles for the gaseous environment used in experiments were validated by detailed CFD calculations. For both metals, the particle combustion times could be approximately described by D^n law; the exponent n was close to 0.64 for aluminum and to 0.68 for magnesium. The results deviate substantially from earlier experimental data for both metals burning in water; there is also substantial

discrepancy with a popular empirical correlation [23] proposed for aluminum burn times. The measured burn times are longer than implied by previous work employing coarse powders; this discrepancy is attributed to differences in both transport and chemical reaction mechanisms for fine metal particles. The present results are qualitatively consistent with recently reported trends describing burn time as a function of particle size for fine aluminum particles burning in oxygen and other oxidizers [32, 33, 64, 65].

In Chapter 3, burn times and temperatures were measured optically for a set of mechanically alloyed, micron-sized Al·Mg powders injected into a laminar and a turbulent air-acetylene flame. The measured trends for burn times, t, as a function of particle size, d, for all alloys were described by a $t=a\cdot d^n$ law where the exponent n varied from 0.6 to 1. Shorter burn times were measured in more turbulent flows; respectively, the values of pre-exponent, a, decreased and exponent, n, increased slightly with an increased level of turbulence. An increase in Mg concentration led to longer burn times for the alloy particles for all flame conditions. For all compositions, alloy particles burned longer than similarly sized Al particles except for the alloy with the smallest concentration of Mg, $Al_{0.9}Mg_{0.1}$, for which particles less than ca. 4 μm burned faster than similarly sized Al. This effect was observed for laminar and turbulent flames. The burn times measured here were longer compared to the burn times measured for the same alloy particles ignited by the CO_2 laser beam and burning in a quiescent room air. This is attributed to different oxidizing efficiencies of the CO_2/H_2O mixture used here compared to O_2 present in air. The optically measured temperatures were lower for $Al_{0.47}Mg_{0.53}$ alloy (~ 2400 K) compared to ~ 2700 – 2800 K obtained for other alloys. Turbulent mixing resulted in a slight increase in the measured temperature. The temperatures were

not appreciably affected by the particle sizes. The results can be qualitatively interpreted considering that an increase in the Mg concentration leads to an accelerated vapor phase reaction; at the same time it can lead to the accelerated condensation of MgO crystallites on the particle surface. The surface MgO may impede evaporation of Al or its surface reaction with a gaseous oxidizer, leading to longer burn times. For some flame conditions, the surface MgO can be heated above the Mg or Al boiling points. This could affect both temperature measurements and heat transfer to the burning alloy particle.

REFERENCES

1. Price, E.W., *Combustion of aluminum in solid propellant flames.* AGARD (Advisory Group for Aerospace Research and Development) Conference Proceedings, (259): p. 14. 1-14. 15.

2. Davis, A., *Solid propellants: The combustion of particles of metal ingredients.* Combustion and Flame, 1963. **7**(1): p. 359-367.

3. De Luca, L.T., et al. *Dual-oxidizer metallized solid propellants for low-cost space access*. 57th International Astronautical Congress, 2006. Valencia.

4. Frost, D.L. and F. Zhang, *Nonideal blast waves from heterogeneous explosives*, S. Itoh, K. Hokamoto, and M. Fujita, Editors. Proceedings of 1st International Symposium on Explosion, Shock Wave and Hypervelocity Phenomena, 2004. Kumamoto, Japan. p. 421-426.

5. Grishkin, A.M., et al., *The influence of admixtures of powder-like aluminium on detonation parameters of high-order explosive systems.* Fizika Goreniya i Vzryva, 1993. **29**(2): p. 115-117.

6. Jones, H.D. and F.J. Zerilli. *Reaction kinetics of metallized explosives*. 1993. Publ by Materials Research Society.

7. Miller, P.J. and R.H. Guirguis. *Experimental study and model calculations of metal combustion in Al/AP underwater explosives*. 1993. Publ by Materials Research Society.

8. Carney, J.R., et al., *Time-resolved optical measurements of the post-detonation combustion of aluminized explosives.* Review of Scientific Instruments, 2006. **77**(6).

9. Kim, C.K., et al. *Afterburning of TNT explosive products in air with aluminum particles*. 46th AIAA Aerospace Sciences Meeting, 2008. Reno, NV.

10. Rajendran, A.G., C.B. Kartha, and V.V. Babu, *Burn rate studies of a titanium-based pyrotechnic smoke composition.* Defence Science Journal, 2000. **50**(2): p. 199-206.

11. Gillard, P. and M. Roux, *Study of the radiation emitted during the combustion of pyrotechnic charges. Part I: Non stationary measurement of the temperature by means of a two-color pyrometer.* Propellants, Explosives, Pyrotechnics, 2002. **27**(2): p. 72-79.

12. Ba, S.H., Q.J. Jiao, and H. Ren, *Effect of particle sizes of aluminum powder on radiation intensity of flash pyrotechnic composites.* Hanneng Cailiao/Chinese Journal of Energetic Materials, 2008. **16**(2): p. 219-221.

13. Smit, K.J., et al., *Infrared-emitting species identified in the combustion of boron-based pyrotechnic compositions.* Applied Spectroscopy, 1997. **51**(9): p. 1400-1404.

14. Gogulya, M.F., et al., *Explosive characteristics of aluminized HMX-based nanocomposites.* Combustion, Explosion and Shock Waves, 2008. **44**(2): p. 198-212.

15. Frost, D.L., et al. *Reaction of titanium and zirconium particles in cylindrical explosive charges*. AIP Conference Proceedings, 2007. Waikoloa, HI.

16. Goroshin, S., et al., *Optical pyrometry of fireballs of metalized explosives.* Propellants, Explosives, Pyrotechnics, 2006. **31**(3): p. 169-181.

17. Gogulya, M.F., et al., *Mechanical sensitivity and detonation parameters of aluminized explosives.* Combustion, Explosion and Shock Waves, 2004. **40**(4): p. 445-457.

18. Yeh, C.L., M.M. Mench, and K.K. Kuo, *An investigation on flame-spreading process of thin film Mg/PTFE/Mg pyrotechnics.* Combustion Science and Technology, 1997. **126**(1-6): p. 271-289.

19. Miller, P.J. *Reactive flow model with coupled reaction kinetics for detonation and combustion in non-ideal explosives*. 1996. Boston, MA, USA: Materials Research Society.

20. Chidester, S.K., et al., *On the violence of thermal explosion in solid explosives.* Combustion and Flame, 1997. **110**(1-2): p. 264-280.

21. Yoh, J.J.I., et al. *Test-based thermal explosion model for HMX*. Proceedings of the Combustion Institute, 2007. **31**(2): p. 2353-2359.

22. Manner, V.W., et al., *The role of aluminum in the detonation and post-detonation expansion of selected cast HMX-based explosives.* Propellants, Explosives, Pyrotechnics, 2012. **37**(2): p. 198-206.

23. Beckstead, M.W., *Correlating aluminum burning times.* Combustion, Explosion and Shock Waves, 2005. **41**(5): p. 533-546.

24. Cashdollar, K.L., *Overview of dust explosibility characteristics.* Journal of Loss Prevention in the Process Industries, 2000. **13**(3-5): p. 183-199.

25. Pu, Y.K., et al., *Turbulence effects on dust explosions in the 20-liter spherical vessel.* Symposium (International) on Combustion, 1991. **23**(1): p. 843-849.

26. Chen, Z. and B. Fan, *Flame propagation through aluminum particle cloud in a combustion tube.* Journal of Loss Prevention in the Process Industries, 2005. **18**(1): p. 13-19.

27. Kuhl, A.L., P. Neuwald, and H. Reichenbach, *Effectiveness of combustion of shock-dispersed fuels in calorimeters of various volumes.* Combustion, Explosion and Shock Waves, 2006. **42**(6): p. 731-734.

28. Birouk, M. and I. Gökalp, *Current status of droplet evaporation in turbulent flows.* Progress in Energy and Combustion Science, 2006. **32**(4): p. 408-423.

29. Bradley, D., Z. Chen, and J.R. Swithenbank, *Burning rates in turbulent fine dust-air explosions.* Symposium (International) on Combustion, 1989. **22**(1): p. 1767-1775.

30. Kumar, R.K., E.M. Bowles, and K.J. Mintz, *Large-scale dust explosion experiments to determine the effects of scaling on explosion parameters.* Combustion and Flame, 1992. **89**(3-4): p. 320-332.

31. Lynch, P., H. Krier, and N. Glumac. *A correlation for burn time of aluminum particles in the transition regime*. Proceedings of the Combustion Institute, 2009. **32**(2): p. 1887-1893.

32. Badiola, C., R.J. Gill, and E.L. Dreizin, *Combustion characteristics of micron-sized aluminum particles in oxygenated environments.* Combustion and Flame, 2011. **158**(10): p. 2064-2070.

33. Gill, R.J., C. Badiola, and E.L. Dreizin, *Combustion times and emission profiles of micron-sized aluminum particles burning in different environments.* Combustion and Flame, 2010. **157**(11): p. 2015-2023.

34. Gill, R.J., S. Mohan, and E.L. Dreizin, *Sizing and burn time measurements of micron-sized metal powders.* Review of Scientific Instruments, 2009. **80**(6): p. 064101-1 – 064101-7.

35. Miller, T. and J. Herr, *Green rocket propulsion by reaction of Al and Mg powders and water*, in *40th AIAA/ASME/SAE/ASEE Joint Propulsion Conference and Exhibit*. 2004, American Institute of Aeronautics and Astronautics.

36. Foote J. P. , T.B.R., Lineberry J. T. , *Combustion of aluminum and steam for underwater propulsion*, in *Advances in Chemical Propulsion : Science to Technology*, G.D. Roy, Editor. 2002. p. 133 - 147.

37. Sippel, T.R., T.L. Pourpoint, and S.F. Son, *Combustion of nanoaluminum and water propellants: effect of equivalence ratio and safety/aging characterization.* Propellants, Explosives, Pyrotechnics, 2013: p. n/a.

38. Pourpoint, T.L., et al., *Feasibility study and demonstration of an aluminum and ice solid propellant.* International Journal of Aerospace Engineering, 2012. **2012**: p. 11.

39. Risha, G., et al., *Aluminum-ICE (ALICE) propellants for hydrogen generation and propulsion*, in *45th AIAA/ASME/SAE/ASEE Joint Propulsion Conference & Exhibit*. 2009, American Institute of Aeronautics and Astronautics.

40. Diwan, M., et al., *Combustion wave propagation in magnesium/water mixtures: experiments and model.* Chemical Engineering Science, 2010. **65**(1): p. 80-87.

41. Petrovic, J. and G. Thomas, *Reaction of aluminum with water to produce hydrogen*, U.S.D.O. Energy, Editor. 2008, U.S. Department Of Energy.

42. Wang, H.Z., et al., *A review on hydrogen production using aluminum and aluminum alloys.* Renewable and Sustainable Energy Reviews, 2009. **13**(4): p. 845-853.

43. Vlaskin, M.S., et al., *An experimental aluminum-fueled power plant.* Journal of Power Sources, 2011. **196**(20): p. 8828-8835.

44. Franzoni, F., et al., *Operating maps of a combined hydrogen production and power generation system based on aluminum combustion with water.* International Journal of Hydrogen Energy, 2011. **36**(4): p. 2803-2816.

45. Mercati, S., et al., *Design of the steam generator in an energy conversion system based on the aluminum combustion with water.* Applied Energy, 2012. **97**(0): p. 686-694.

46. Dupiano, P., D. Stamatis, and E.L. Dreizin, *Hydrogen production by reacting water with mechanically milled composite aluminum-metal oxide powders.* International Journal of Hydrogen Energy, 2011. **36**(8): p. 4781-4791.

47. Nie, H., M. Schoenitz, and E.L. Dreizin, *Calorimetric investigation of the aluminum–water reaction.* International Journal of Hydrogen Energy, 2012. **37**(15): p. 11035-11045.

48. Gai, W.-Z., et al., *Reaction of Al powder with water for hydrogen generation under ambient condition.* International Journal of Hydrogen Energy, 2012. **37**(17): p. 13132-13140.

49. Yang, W., et al., *Theoretical study on the reaction of magnesium with water in the gas-phase.* International Journal of Hydrogen Energy, 2011. **36**(17): p. 10608-10613.

50. Grosjean, M.H., et al., *Hydrogen production via hydrolysis reaction from ball-milled Mg-based materials.* International Journal of Hydrogen Energy, 2006. **31**(1): p. 109-119.

51. Ozerov, E.S. and A.A. Yurinov, *Combustion of particles of aluminum-magnesium alloys in water vapor.* Combustion, Explosion and Shock Waves, 1977. **13**(6): p. 778-780.

52. Prachukho, V.P., E.S. Ozerov, and A.A. Yurinov, *Burning of magnesium particles in water vapor.* Combustion, Explosion and Shock Waves, 1971. **7**(2): p. 195-198.

53. Huang, X., et al., *Experimental study on the ignition and combustion characteristics of a magnesium particle in water vapor.* Science China Technological Sciences, 2012. **55**(9): p. 2601-2608.

54. Bazyn, T., H. Krier, and N. Glumac, *Oxidizer and pressure effects on the combustion of 10-μm aluminum particles.* Journal of Propulsion and Power, 2005. **21**(4): p. 577-582.

55. Corcoran, A.L., V.K. Hoffmann, and E.L. Dreizin, *Aluminum particle combustion in turbulent flames.* Combustion and Flame, 2013. **160**(3): p. 718-724.

56. CD-adapco, *USER GUIDE Star CCM+ Version 7.06*, ed. CD-adapco. 2012: CD-adapco. 12179.

57. Veynante, D. and L. Vervisch, *Turbulent combustion modeling.* Progress in Energy and Combustion Science, 2002. **28**(3): p. 193-266.

58. Pope, S.B., *PDF methods for turbulent reactive flows.* Progress in Energy and Combustion Science, 1985. **11**(2): p. 119-192.

59. McBride, B.J., S. Gordon, and M.A. Reno, *Coefficients for calculating thermodynamic and transport properties of individual species*. 1993, National Aeronauitics and Space Administration: Cleveland OH. p. 1-94.

60. Sutherland, W., *The viscosity of gases and molecular force.* Philosophical Magazine (S.5), 1893. **36**: p. 507-531.

61. Menter, F.R., M. Kuntz, and R. Langtry. *Ten years of industrial experience with the SST turbulence model*. in *Turbulence, Heat and Mass Transfer 4*. 2003. Antalya, Turkey.

62. Mohan, S., M.A. Trunov, and E.L. Dreizin, *On possibility of vapor-phase combustion for fine aluminum particles.* Combustion and Flame, 2009. **156**(11): p. 2213-2216.

63. Mohan, S., L. Furet, and E.L. Dreizin, *Aluminum particle ignition in different oxidizing environments.* Combustion and Flame, 2010. **157**(7): p. 1356-1363.

64. Badiola, C. and E.L. Dreizin, *On weak effect of particle size on its burn time for micron-sized aluminum powders.* Combustion Science and Technology, 2012. **184**(12): p. 1993-2007.

65. Dreizin, E.L., et al., *Particle combustion dynamics of metal-based reactive materials* International Journal of Energetic Materials and Chemical Propulsion, 2011. **10**(4): p. 22.

66. Habu, H., *Application of magnalium to solid rocket propellant.* Keikinzoku, 2008. **58**(Copyright (C) 2012 American Chemical Society (ACS). All Rights Reserved.): p. 162-166.

67. De Luca, L.T., et al. *Low-cost and green solid propellants for space propulsion*. 2nd International Conference on Green Propellants for Space Propulsion, 2004. Sardinia, Italy.

68. Price, E.W., *Combustion of metallized propellants*. Progress in Astronautics and Aeronautics, ed. K.K.K.a.M. Summerfield. Vol. 90. 1984, New York: AIAA. 479-513.

69. Zarei, Z. and D.L. Frost, *Simplified modeling of blast waves from metalized heterogeneous explosives.* Shock Waves, 2011. **21**(5): p. 425-438.

70. Nacu, S., *Practical aspects on using polytetrafluorethylene (PTFE) in pyrotechnic compositions.* Revista de Chimie, 2011. **62**(1): p. 113-115.

71. Zenin, A.A., G.P. Kuznetsov, and V.I. Kolesnikov, *Combustion of aluminum-magnesium alloy particles in micro gravity.* Khim. Fiz., 2011. **30** American Chemical Society (ACS). (Translated 2012): p. 28-41.

72. Roberts, T.A., R.L. Burton, and H. Krier, *Ignition and combustion of aluminum/magnesium alloy particles in oxygen at high pressures.* Combust. Flame, 1993. **92** American Chemical Society (ACS). (Translated 2012): p. 125-143.

73. Breiter, A.L., E.I. Popov, and V.L. Velikanova, *Combustion of aluminum, magnesium, and their alloys in steam at high pressures.* Fiz. Aerodispersnykh Sist., 1983. **23** American Chemical Society (ACS). (Translated 2012): p. 43-48.

74. Yuasa, S. and T. Takeno, *Ignition and combustion of magnesium-aluminum alloy particle clouds in a hot gas stream.* Symp. (Int.) Combust., [Proc.], 1982. **19th** American Chemical Society (ACS). (Translated 2012): p. 741-748.

75. Popov, E.I., et al., *Mechanism of combustion of aluminum-magnesium alloy particles.* Fiz. Goreniya Vzryva, 1973. **9** American Chemical Society (ACS). (Translated 2012): p. 240-246.

76. Breiter, A.L., et al., *Combustion of single particles of aluminum-magnesium alloys in the flame of an oxidizing agent-fuel mixture.* Fiz. Goreniya Vzryva, 1971. **7** American Chemical Society (ACS). (Translated 2012): p. 222-227.

77. Poyarkov, V.G., *Combustibility of aluminum-magnesium powdered alloys.* Izv. Vyssh. Ucheb. Zaved., Tsvet. Met., 1967. **10** American Chemical Society (ACS). (Translated 2012): p. 149-153.

78. Aly, Y., M. Schoenitz, and E.L. Dreizin, *Ignition and combustion of mechanically alloyed Al-Mg powders with customized particle sizes.* Combustion and Flame, 2013. **160**(4): p. 835-842.

79. Schoenitz, M. and E. Dreizin, *Oxidation processes and phase changes in metastable Al-Mg alloys.* Journal of Propulsion and Power, 2004. **20**(6): p. 1064-1068.

80. Schoenitz, M. and E.L. Dreizin, *Structure and properties of Al-Mg mechanical alloys.* Journal of Materials Research, 2003. **18**(8): p. 1827-1836.

81. Shoshin, Y.L., R.S. Mudryy, and E.L. Dreizin, *Preparation and characterization of energetic Al-Mg mechanical alloy powders.* Combustion and Flame, 2002. **128**(3): p. 259-269.

82. Ozerov, E.S. and A.A. Yurinov, *Combustion of particles of aluminum-magnesium alloys in water vapor.* Combustion, Explosion, and Shock Waves, 1978. **13**(6): p. 778-780.

83. Corbel, J.M.L., et al., *Strobes: An oscillatory combustion.* Journal of Physical Chemistry B, 2012. **116**(16): p. 4967-4975.

84. Disimile, P.J. and N. Toy, *Examining the potential fire risk from a short duration pyrotechnic event.* Fire Technology, 2008. **44**(1): p. 77-96.

85. Ganesh, D. and G. Gowrishankar. *Effect of nano-fuel additive on emission reduction in a biodiesel fuelled CI engine*. in *2011 International Conference on Electrical and Control Engineering, ICECE 2011 - Proceedings*. 2011.

86. Habu, H., *Application of magnalium to solid rocket propellant.* Keikinzoku/Journal of Japan Institute of Light Metals, 2008. **58**(4): p. 162-166.

87. Habu, H. and K. Hori, *The burning rate characteristics of magnalium (Mg/Al)-AP based solid propellant.* Science and Technology of Energetic Materials, 2006. **67**(6): p. 187-192.

88. Liu, T.K., I.M. Shyu, and Y.S. Hsia, *Effect of fluorinated graphite on combustion of boron and boron-based fuel-rich propellants.* Journal of Propulsion and Power, 1996. **12**(1): p. 26-33.

89. Murata, H., et al., *Effect of magnalium (Mg-Al alloy) on combustion characteristics of ammonium nitrate-based solid propellant.* Kayaku Gakkaishi/Journal of the Japan Explosives Society, 2000. **61**(2): p. 58-66.

90. Obuchi, K., M. Tanabe, and T. Kuwahara. *Ignition characteristics of boron particles in the secondary combustor of ducted rockets -effects of magnalium particle addition*. in *46th AIAA Aerospace Sciences Meeting and Exhibit*. 2008.

91. Aly, Y., et al., *Reactive, mechanically alloyed Al · Mg powders with customized particle sizes and compositions.* Journal of Propulsion and Power, 2014. **30**(1): p. 96-104.

92. Egorov, A.G., E.D. Kal'nej, and A.P. Shajkin, *Flame stabilization of powder metal fuel in turbulent air flow.* Fizika Goreniya i Vzryva, 2001. **37**(5): p. 28-35.

93. Corcoran, A., et al., *Combustion of fine aluminum and magnesium powders in water.* Combustion and Flame, 2013. **160**(10): p. 155-160.

94. Krier, H. and N. Glumac, *On the transition from classical diffusion-limited combustion behavior for fine and ultrafine aluminum particles.* International Journal of Energetic Materials and Chemical Propulsion, 2009. **8**(1): p. 71-80.

95. Lynch, P., H. Krier, and N. Glumac, *A correlation for burn time of aluminum particles in the transition regime.* Proceedings of the Combustion Institute, 2009. **32 II**: p. 1887-1893.

96. Badiola, C. and E.L. Dreizin, *Combustion of micron-sized particles of titanium and zirconium.* Proceedings of the Combustion Institute, 2013. **34**(2): p. 2237-2243.

97. Ermoline, A., D. Yildiz, and E.L. Dreizin, *Model of heterogeneous combustion of small particles.* Combustion and Flame, 2013.

98. Chase, M.W., *NIST-JANAF Themochemical tables, Fourth Edition.* J. Phys. Chem. Ref. Data, Monograph 9, 1998: p. 1-1951.